Neutron-capture element abundances in the planetary nebula NGC 5315 from deep optical and near-infrared spectrophotometry[*][†]

S. Madonna,[1,2][‡] J. García-Rojas,[1,2] N. C. Sterling,[3] G. Delgado-Inglada,[4]
A. Mesa-Delgado,[5] V. Luridiana,[1,2] I. U. Roederer[6,7] and A. L. Mashburn[3]

[1]*Instituto de Astrofísica de Canarias, E-38205 La Laguna, Tenerife, Spain*
[2]*Dpto. Astrofísica, Universidad de La Laguna, E-38206 La Laguna, Tenerife, Spain*
[3]*Department of Physics, University of West Georgia, 1601 Maple Street, Carrollton, GA 30118, USA*
[4]*Instituto de Astronomía, Universidad Nacional Autónoma de México, Apdo. Postal 70264, Ciudad de México 04510, Mexico*
[5]*Instituto de Astrofísica, Facultad de Física, Pontificia Universidad Católica de Chile, Av. Vicuña Mackenna 4860, 782-0436 Macul, Santiago, Chile*
[6]*Department of Astronomy, University of Michigan, 1085 South University Avenue, Ann Arbor, MI 48109, USA*
[7]*Joint Institute for Nuclear Astrophysics and Center for the Evolution of the Elements (JINA-CEE), USA*

ABSTRACT

We analyse the chemical composition of the planetary nebula (PN) NGC 5315, through high-resolution ($R \sim 40000$) optical spectroscopy with Ultraviolet-Visual Echelle Spectrograph at the Very Large Telescope, and medium-resolution ($R \sim 4800$) near-infrared spectroscopy with Folded-port InfraRed Echellette at Magellan Baade Telescope, covering a wide spectral range from 0.31 to 2.50 μm. The main aim of this work is to investigate neutron (n)-capture element abundances to study the operation of the slow n-capture ('s-process') in the asymptotic giant branch (AGB) progenitor of NGC 5315. We detect more than 700 emission lines, including ions of the n-capture elements Se, Kr, Xe and possibly Br. We compute physical conditions from a large number of diagnostic line ratios, and derive ionic abundances for species with available atomic data. The total abundances are computed using recent ionization correction factors (ICFs) or by summing ionic abundances. Total abundances of common elements are in good agreement with previous work on this object. Based on our abundance analysis of NGC 5315, including the lack of s-process enrichment, we speculate that the most probable evolutionary scenario is that the progenitor star is in a binary system as hinted at by radial velocity studies, and interactions with its companion truncated the AGB before s-process enrichment could occur. However there are other two possible scenarios for its evolution, that cannot be ruled out: (i) the progenitor is a low-mass single star that did not undergo third dredge-up; (ii) the progenitor star of NGC 5315 had an initial mass of 3–5 M$_\odot$, and any s-process enhancements were heavily diluted by the massive envelope during the AGB phase.

Key words: stars: AGB and post-AGB – ISM: abundance – planetary nebulae: individual: NGC 5315.

1 INTRODUCTION

Trans-iron (n-capture) elements are produced in asymptotic giant branch (AGB) stars (1–8 M$_\odot$) in the intershell region between the H- and He-burning shells, in the so-called s-process (slow neutron-capture process). In these layers, neutrons are released by α-captures

on to ^{13}C (or ^{22}Ne in AGB stars with mass >3–4 M$_\odot$). During the thermally pulsing phase, convective dredge-up conveys to the stellar surface C and s-process-enriched material, which is then expelled to the interstellar medium in the planetary nebula (hereafter PN) phase and eventually incorporated in a new generation of stars. Thus, the abundances of n-capture elements and the s-process element-by-element enrichment pattern reveal critical information on physical conditions in stellar interiors and the nucleosynthetic histories of stellar populations (Cristallo et al. 2011, 2015; Karakas & Lattanzio 2014; Trippella et al. 2014, 2016; Ventura et al. 2015).

While s-process nucleosynthesis has historically been studied through stellar spectra, nebular spectroscopy presents unique

advantages. PNe allow for the first observational analysis of the lightest *n*-capture elements (Ge, Se and Br) and the noble gases Kr and Xe in one of their sites of origin. A crucial difference from AGB stars is that PNe represent the final envelope abundances of their progenitor stars, after the cessation of nucleosynthesis and dredge-up that occurred during the AGB phase. PN abundances are therefore highly valuable for stellar yield determinations. Moreover, nebular abundance determinations provide key constraints to poorly understood processes in models of stellar evolution and nucleosynthesis, such as the efficiency of third dredge-up (TDU) at low envelope masses, the number of thermal pulses, and treatments of mass-loss and convective overshoot (Karakas et al. 2009; Karakas, García-Hernández & Lugaro 2012; Karakas & Lattanzio 2014; Cristallo et al. 2015; Ventura et al. 2015; Trippella et al. 2016, and references therein). The number of *n*-capture elements that can be detected in individual PNe allows for meaningful comparisons with various sets of evolutionary models (e.g. Sterling et al. 2016, hereafter S16). In particular, the optical region is home to numerous *n*-capture element transitions, including lines from multiple ions of Se, Br, Kr, Rb and Xe that have been detected in various PNe (e.g. Sharpee et al. 2007; García-Rojas et al. 2012, 2015).

Since the pioneering work by Péquignot & Baluteau (1994), only a few detailed studies of n-capture element abundances based on deep, high-resolution optical spectra have been conducted in PNe. Sharpee et al. (2007) identified lines of Br, Kr, Rb, Xe, Ba, and possibly Te and I in four PNe, with 4- and 6-m class telescopes. But at their resolution of ~22 000, many features were not unambiguously detected. García-Rojas et al. (2015) made a detailed *n*-capture element abundance analysis in NGC 3918, a PN with a high ionization degree and with a C/O ratio close to 1, detecting several ions of Kr, Xe, Rb and Se. This allowed them to test the new ionization correction factors (ICFs) for n-capture elements provided by Sterling, Porter & Dinerstein (2015) and to compute total abundances with unprecedented accuracy. In contrast, near-infrared (hereafter NIR) lines of n-capture elements have been studied in a large number of PNe. For example, Sterling & Dinerstein (2008)'s survey of [Kr III] and [Se IV] in 120 PNe resulted in the first overview of s-process enrichments in PNe. However, their abundance determinations were uncertain by factors of 2–3, since only one ion of each element was detected, leading to large and uncertain corrections for unobserved ions.

In this work we combine optical and NIR spectroscopy to study NGC 5315, a PN that has been classified as an almost spherical (slightly elliptical) PN with a complicated structure, including a somewhat broken ring. The H-deficient WC4 central star has a temperature of about 76–79 kK (Marcolino et al. 2007; Todt et al. 2015), which is considerably lower than other early-type [WR] stars (120–150 kK). Several studies have focused on the chemical content in NGC 5315, but draw different conclusions, especially regarding the N/O ratio which is important for constraining the progenitor mass. Pottasch et al. (2002) combined IUE ultraviolet and ISO infrared spectra with optical data to investigate chemical abundances, and found a relatively high N/O ~ 0.88. Milingo et al. (2010) found a very similar value from optical/NIR spectrophotometry, as did Peimbert et al. (2004). The excess of He and N led these authors to classify NGC 5315 as a Peimbert Type I PN (He/H > 0.125 and N/O > 0.5, or N/O > 0.8 Peimbert 1978; Kingsburgh & Barlow 1994), although it is not an extreme object. The high concentration of He and N may be explained with the occurrence of the second dredge-up and CN-cycling during hot bottom burning (HBB), which are activated in AGB stars with $M > 3$–$4\,\mathrm{M}_\odot$ (Becker & Iben 1979; Boothroyd, Sackmann & Ahern 1993; Di

Criscienzo et al. 2016). Karakas & Lugaro (2016) found through detailed theoretical models that HBB activation requires a minimum progenitor mass between 4 and 5 $\mathrm{M}_\odot$.

However, other investigations of NGC 5315 (de Freitas Pacheco et al. 1991; Samland et al. 1992; Tsamis et al. 2003; Dufour et al. 2015) do not find Type I abundances, calling into question whether the PN indeed derives from a more massive progenitor. It should be noted that only N^+ has collisionally excited optical transitions. Since this is a trace ion, the ICF for N can be large and uncertain when only optical data are used in deriving its abundance. The detection of [N III] and [N IV] lines in UV spectra can lead to much more accurate N abundance determinations. Both Tsamis et al. (2003) and Dufour et al. (2015) utilize optical and UV data, finding N/O ratios of 0.54 and 0.41, respectively, contrasting with the much higher value of Pottasch et al. (2002). This variance may illustrate the uncertainties of abundances computed with highly temperature-sensitive UV lines. As for the C/O abundance ratio, the values found in the literature range from 0.35 (Tsamis et al. 2003) to 0.95 (Peimbert et al. 2004). The N/O and C/O ratios are very useful for constraining the progenitor mass, and the disparity in the ratios found, even from UV observations that provide access to a wide range of C and N ions, highlight the enigmatic nature of NGC 5315's progenitor. The different emission lines and methods used to derive C/O and N/O ratios will be discussed in detail in Section 7.

Abundance determinations of *n*-capture elements in PNe can provide more restrictive constraints to the mass of the progenitor star. Observations of emission lines of *n*-capture elements in Type I PNe suggest that they exhibit little if any s-process enrichments (Sterling & Dinerstein 2008; Sterling et al. 2015), although in such studies only one or two *n*-capture elements were studied. On the other hand, very low massive progenitors ($<1.5\,\mathrm{M}_\odot$) will also show little s-process enrichments as they have not gone through the TDU. However Rb enrichments in PNe can help to disentangle this puzzle, because it is an indicator of the main neutron source during the AGB phase (^{13}C or ^{22}Ne) and, hence of the mass of the progenitor star (Busso, Gallino & Wasserburg 1999).

There are relatively few observational constraints on nucleosynthetic models for AGB stars with $M > 3$–$4\,\mathrm{M}_\odot$. García-Hernández et al. (2006, 2009) reported large Rb enrichments in 4–8 $\mathrm{M}_\odot$ Galactic and Magellanic cloud AGB stars, respectively. García-Hernández et al. (2007, 2013) provided Zr and Rb abundances, respectively, for massive Galactic AGB stars; however, they found extremely high Rb/Zr ratios that were not predicted by nucleosynthesis models. Zamora et al. (2014) took into account circumstellar effects to compute Rb/Zr values in better agreement with results from AGB nucleosynthesis models for stars with masses between 4 and 8 $\mathrm{M}_\odot$ ($-0.2 \leq$ [Rb/Zr] < 0.6) (Karakas et al. 2012). According to the models of Karakas et al. (2012), Kr and Se should be enriched in the objects which show Rb enrichment for the ^{22}Ne neutron source. Therefore, deep optical and NIR spectroscopy of PNe, with the aim of detecting emission lines of Rb, Kr and Se of different ionization stages, is a very valuable tool to improve the accuracy of these n-capture element abundance determinations and hence better constrains the initial mass of the progenitor stars of these objects.

This study is a continuation of our work to collect deep, high-resolution spectra of PNe to investigate objects covering different ionization degrees to detect as many ions as possible of *n*-capture elements in order to improve the accuracy of their abundance determinations. These observations aim to address scientific goals including (i) to study the correlation between different *n*-capture elements and C enrichment, predicted by models; (ii) to study the

Table 1. Journal of observations.

Telescope	Date	Δλ (Å)	Exp. time (s)	Seeing (arcsec)
8.2 m VLT	2014/01/02	B1: 3100–3885	60, 2 × 630	<1.1
"	"	B2: 3750–4995	60, 2 × 630	<1.1
"	"	R1: 4785–6805	60, 2 × 630	<1.1
"	"	R2: 6700–10420	60, 2 × 630	<1.1
"	2014/02/03	B1: 3100–3885	6 × 630	<1.5
"	"	B2: 3750–4995	6 × 630	<1.5
"	"	R1: 4785–6805	6 × 630	<1.5
"	"	R2: 6700–10420	6 × 630	<1.5
"	2014/02/04	B1: 3100–3885	4 × 630	<1.4
"	"	B2: 3750–4995	4 × 630	<1.4
"	"	R1: 4785–6805	4 × 630	<1.4
"	"	R2: 6700–10420	4 × 630	<1.4
6.5 m MBT	2013/08/13	8000–25000	20 × 30	1.8–2.9

correlation between the pattern of *n*-capture element abundances and the mass of the progenitor star, which is modulated by the nuclear reaction activated in each mass range (Karakas et al. 2012; van Raai et al. 2012); (iii) to use detections of multiple ions of individual *n*-capture elements to test the atomic data and ICF prescriptions (Sterling et al. 2015) for these species. Our first results for NGC 3918 have been published by García-Rojas et al. (2015).

The observations and data reduction are described in Section 2. The identification of lines and reddening correction is presented in Section 3. In Section 4, we compute the physical conditions. In Sections 5 and 6, we compute ionic and total abundances. In Section 7 we discuss the results and in Section 8 we draw some conclusions.

2 OBSERVATIONS AND DATA REDUCTION

2.1 UVES

The optical spectra of NGC 5315 were taken with the Ultraviolet-Visual Echelle Spectrograph (UVES; D'Odorico et al. 2000), attached to the 8.2m Kueyen (UT2) Very Large Telescope at Cerro Paranal Observatory (Chile) in service mode. The observations were performed during three nights under clear/dark conditions and the seeing remained below 1.5 arcsec during the whole run (see Table 1).

The slit width was set to 1 arcsec, which provides an effective spectral resolution $R \sim 40\,000$. See García-Rojas et al. (2015) for further details on the instrument setup. The journal of observations is shown in Table 1. The atmospheric dispersion corrector was used to compensate for atmospheric dispersion. The UVES spectra are divided in four spectral ranges (B1, B2, R1 and R2). We took individual exposures of 630 s in each configuration and we followed the same sequence as in García-Rojas et al. (2015). After combining all the extracted spectra, we obtained a total exposure time of 2.10 h in each configuration. Additional single short exposures of 60 s during the first night were taken to obtain non-saturated flux measurements for the brightest emission lines. Reduction of the raw frames was done in the same way as in García-Rojas et al. (2015) for each night. The extracted spectra cover an area of 3.95 arcsec × 1 arcsec common to all spectral ranges. Spectrophotometric standards Feige 67 (Oke 1990) and LTT 3218 (Hamuy et al. 1992, 1994) were observed to perform the flux calibration and were also fully reduced with the
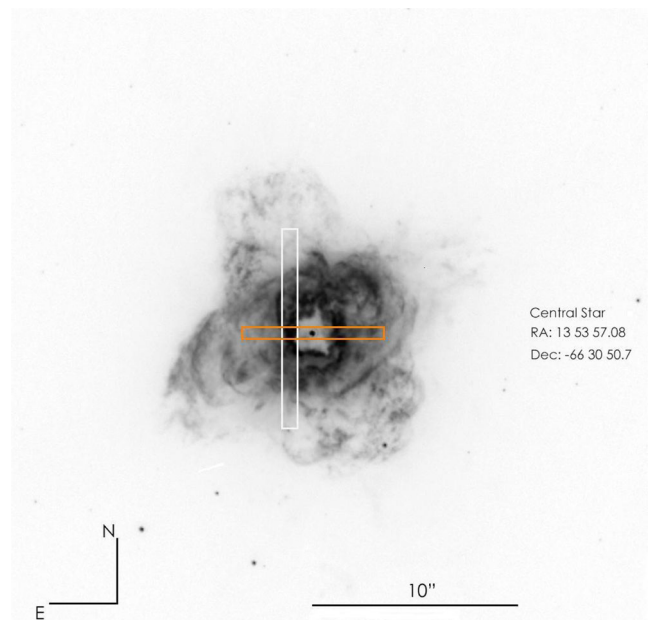
Figure 1. Deep *Hubble Space Telescope* (*HST*) Hα image of NGC 5315. Position and coordinate of the central star are shown. The N–S slit position for UVES observation is indicated as a white rectangular box, while the orange rectangular box represents the E–W slit for FIRE observation.

pipeline. We used IRAF[1] (Tody 1993) to perform the flux calibration and the radial velocity (RV) corrections. Flux-calibrated, RV corrected, one-dimensional spectra for each night were finally co-added to obtain the final one-dimensional optical spectra analyses in this paper.

In Fig. 1 we show a high spatial resolution Hα image of NGC 5315 from the *HST* archive. The slit centre was set 1.0 arcsec east to the central star of NGC 5315 oriented N–S (PA = 0°), covering the brightest area of NGC 5315.

2.2 FIRE

The NIR spectra of NGC 5315 were taken with the Folded-port InfraRed Echellette (FIRE, Simcoe 2013) spectrograph attached to the 6.5 m Magellan Baade Telescope (MBT) located at Las Campanas Observatory in Chile. The observations were performed on 2013 August 13 and the seeing oscillated between 1.8 and 2.9 arcsec during the run.

The slit that was located across the central star (PA = 90°) (see Fig. 1) is 7 arcsec long with a width of 0.75 arcsec, which leads to a resolution of $R \sim 4800$. The spectral range is 0.8–2.5 μm, which covers *J*, *H* and *K* bands. Wavelength calibrations were performed in vacuum using a Th–Ar lamp, instead of the air wavelengths used in the UVES observations. Unfortunately, the lack of lines in the Th–Ar lamps at wavelengths larger than 2.3 μm led to a poor wavelength solution for the range 2.3–2.5 μm; however, as this range is dominated by the Pfund H I series, this did not affect the identification of the emission lines. For flux calibration and telluric correction, A0V standard stars were observed. We took 20 exposures of 30 s, which led to a total integration time of 600 s. We

---

[1] IRAF is distributed by the National Optical Astronomy Observatories, which are operated by the Association of Universities for Research in Astronomy, Inc., under cooperative agreement with the National Science Foundation.

obtained 20 sky frames nodded 60 arcsec along the slit direction, in order to subtract telluric features from the final spectra. Data reduction was performed with the FIRE reduction software package, FIREHOSE, using optimal extraction. This pipeline is based on the MASE pipeline for the MagE spectrograph (Bochanski et al. 2009), and a brief description of its performance can be found in Simcoe (2013). The journal of observations is shown in Table 1.

3 LINE FLUXES, LINE IDENTIFICATION AND EXTINCTION CORRECTION

The line fluxes were measured with the *splot* routine of the IRAF package. As in García-Rojas et al. (2015), we decided to integrate over the entire line profile as set between two limits over a local continuum estimated by eye, as opposed to fitting an analytic function (such as a Gaussian) to the line profile. The UVES spectra present many misleading features such as telluric lines and internal reflections caused by the dichroic. For this reason, we had to take care to correctly distinguish nebular emission lines. Telluric emission lines are easily recognized and discarded, thanks to their peculiar shape in the 2D spectra (narrow profile and homogeneous emission along the slit). For the weakest telluric features, we used two catalogues: Hanuschik (2003) in the optical and Oliva et al. (2015) in the NIR. When emission line intensities were affected by internal reflections or telluric absorption/emission, we include a note of caution in the line identification tables (Tables 2 and 3).

The UVES spectrum covers four spectral ranges, which overlap at the edges. In order to create a homogeneous set of data, we used the H9 λ3835 line, which lies in the overlapping region between the two spectral ranges B1 and B2, to normalize the line intensities, which were later re-scaled to H β. Lines in the B2 and R1 ranges were directly scaled to H β which is present in both ranges. [S II] $\lambda\lambda$6716 and 6730 Å are the only lines common to the R1 and R2 settings. Unfortunately, in the R2 range, they lie at the extreme blue edge of the spectrum and their fluxes are not reliable. Therefore, we could not re-scale the fluxes in R2 to H β and we normalized all the lines to P7 10 047 Å. The NIR FIRE spectrum does not include the H β line, thus we used a different H I line in each three spectral bands to normalize the line fluxes: P7 10 047 Å for the *J* band, Br10 1.7367 μm for the *H* band and Brγ 2.1661 μm for the *K* band.

For the reddening correction, we assumed the extinction law of Cardelli, Clayton & Mathis (1989) with $R_v = 3.1$. Using Balmer lines from UVES spectra, we found a value of $c(\mathrm{H}\beta) = 0.63 \pm 0.02$. The deepest study of this object in the optical range until now is that of Peimbert et al. (2004), which find a value of $c(\mathrm{H}\beta) = 0.74 \pm 0.04$; while other results from optical data give values in better agreement with our calculation: Dufour et al. (2015) find $c(\mathrm{H}\beta) = 0.56$ from Space Telescope Imaging Spectrograph (STIS)/*HST* data and Cahn, Kaler & Stanghellini (1992) compute $c(\mathrm{H}\beta) = 0.60$. Since a normalization to H β is not available for the spectral range R2 of UVES and for the *J* band of the FIRE spectrum, we considered the extinction coefficient relative to P7 10 047 Å, $c(\mathrm{P7}) = 0.05 \pm 0.01$, calculated assuming the extinction law by Cardelli et al. (1989) with $R_v = 3.1$. Finally, for the *H* band and the *K* band we used the theoretical ratios between the intensities of the reference lines used in each band (Br10 for the *H* band and Brγ for the *K* band) and H β, provided by Storey & Hummer (1995) with $n_e = 30\,000$ cm^{-3} and $T_e = 10\,000$ K, in order to re-scale the final intensities to H β.

We have detected about 700 emission lines. Many are permitted lines of H I, He I, O I, O II, N II, C I, C II, S III, Ne I, Ne II, Mg II and Si II. We also detect several forbidden and semi-forbidden lines from ions such as [N I], [N II], [O I], [O II], [O III], [Ne III], Mg I], [P II], [S II],

[S III], [Cl II], [Cl III], [Cl IV], [Ar III], [Ar IV], [Cr II], [Cr III], [Mn III], [Fe II], [Fe III], [Kr III], [Kr IV], [Se III], [Se IV] and possibly [Xe IV] and [Br III]. In the NIR spectrum, we also detect some molecular H$_2$ 1–0 transitions, but there are no signs of vibrationally excited H$_2$ lines. The depth of our spectra allows us to detect lines as faint as $10^{-5} \times I(\mathrm{H}\beta)$ and $10^{-3} \times I(\mathrm{Br}\gamma)$ in the optical and NIR spectra, respectively. The identifications and adopted laboratory wavelengths of the lines are based on several previous identifications in the literature (e.g. Hora & Latter & Deutsch 1999; Rudy et al. 2001; Peimbert et al. 2004; García-Rojas et al. 2015, and references therein). We also made use of Peter van Hoof's atomic line list v2.05B18.[2] Details on the identification of n-capture element emission lines are given in Section 3.1.

To determine the line flux uncertainties, we considered individually each spectral range (B1, B2, R1 and R2) for UVES and the entire FIRE spectrum. Several lines were chosen in each of these ranges covering the whole range of measured fluxes, i.e. $10^{-5} \leq F(\lambda)/F(\mathrm{H}\beta) \leq 10$; uncertainties in individual fluxes were determined by choosing the highest and lowest reasonable values for the continuum by about 1σ for the selected lines. To assign an error to the whole set of emission lines, we made a logarithmic interpolation between relative intensities and measured uncertainties. An error of 5 per cent for the flux calibration was added quadratically to all line flux uncertainties. In the final intensity uncertainties, we also took in account the error for the extinction correction. Line intensities and identifications are presented in Table 2 for the UVES spectrum and in Table 3 for the FIRE spectrum.

In order to deblend lines with almost coincident central wavelengths, we computed a model using CLOUDY v.13.03 (Ferland et al. 2013) to predicted line fluxes. Stellar temperature and luminosity, nebular diameter and elemental abundances of common elements were optimized to reproduce observed lines in the optical/NIR range from our data and select UV/IR lines from the Pottasch et al. (2002) spectra. The parameters obtained are very similar to those shown in table 2 of Sterling et al. (2015). The model considers the whole PN, since we did not attempt to simulate an observation with a slit located on the PN. We believe this is a reasonable assumption owing to the fact that our slits cover all the ionization zones of the nebula. In Table 4, we compare different diagnostic ratios predicted by our photoionization model to the observed ones. In general, the agreement between observed and predicted ratios is very good.

3.1 Identification of n-capture ion lines

As n-capture elements have very low abundances (Asplund et al. 2009), their lines are very weak. This is why their detection in nebulae has always been a difficult task. However, since the pioneering work by Péquignot & Baluteau (1994), this field has grown significantly. Several *n*-capture element lines (particularly those of Kr, Xe and Se) have been detected in Galactic PNe and H II regions, both in the optical (e.g. García-Rojas et al. 2015, and references therein) and in the NIR (e.g. Dinerstein 2001; Blum & McGregor 2008; Sterling & Dinerstein 2008), and even in other galaxies (Vanzi et al. 2008; Mashburn et al. 2016).

We identify lines of the n-capture element ions [Kr III], [Kr IV], [Se III], [Se IV] and possibly [Xe IV] and [Br III] in NGC 5315 (see Fig. 2). The measured fluxes are shown in Table 5. Below, we give

---

[2] http://www.pa.uky.edu/~peter/newpage/

Table 2. Observed and reddening corrected line ratios [$F(\mathrm{H}\beta) = 100$] and line identifications in NGC 5315.

λ_0 (Å)	Ion	Mult.	λ_{obs}	V_{rad} (km s^{-1})	$F(\lambda)/F(\mathrm{H}ref)^d$	$I(\lambda)/I(\mathrm{H}\beta)^e$	Err (%)^f	Notes
3109.18	[Ar III]	2F	3108.70	−46.28	0.132	0.276	14	
3187.84	He I	3	3187.31	−49.84	1.240	2.453	10	
3218.19	Ne II	4D$_0$-4F	3217.71	−44.71	0.0741	0.144	16	
3244.00	O II	4P-D[2]$_0$	3243.40	−55.45	0.0615	0.117	18	?
3258.27	He I	1S-1P$_0$	3257.79	−44.16	0.0401	0.0757	22	
3296.77	He I	9	3296.22	−50.01	0.0363	0.0671	23	
3323.74	Ne II	7	3323.32	−37.88	0.0287	0.0524	27	
3328.72	N II	3D-3P$_0$	3328.39	−29.72	0.0461	0.0839	20	
3331.31	N II	3D-3P$_0$	3330.81	−45.00	0.0175	0.0318	36	
3334.87	Ne II	2	3334.35	−46.75	0.0885	0.161	15	
3342.50	[Ne III]	2F	3342.30	−17.94	0.103	0.186	14	
3342.85	[Cl III]	2F	*	*	*	*	*	
3353.21	[Cl III]	2F	3352.73	−42.91	0.0293	0.0527	23	
3354.42	He I	8	3354.20	−19.66	0.127	0.228	14	
3367.05	Ne II	12	3366.73	−28.49	0.0255	0.0455	28	
	?		3417.17		0.0191	0.0334	34	
3418.83	[Mn III]	a6S-a4P	*		*	*	*	
3422.82	[Mn III]	a6S-a4P	3422.37	−39.41	0.0162	0.0283	37	
3427.47	[Mn III]	a6S-a4P	3427.07	−34.99	0.0267	0.0466	27	
3434.29	He I	3P$_0$-3D	3433.82	−41.03	0.0086	0.0150	:	
3435.21	He I	3P$_0$-3D	3434.72	−42.76	0.0098	0.0170	:	
3436.22	He I	3P$_0$-3D	3435.73	−42.75	0.0135	0.0236	:	
3437.34	He I	3P$_0$-3D	3436.83	−44.48	0.0197	0.0342	33	
3438.71	He I	3P$_0$-3D	3438.26	−39.23	0.0133	0.0231	:	
3439.99	He I	3P$_0$-3D	3439.56	−37.47	0.0115	0.0200	:	
3441.56	He I	3P$_0$-3D	3441.12	−38.33	0.0110	0.0192	:	
3443.33	He I	3P$_0$-3D	3442.88	−39.18	0.0138	0.0240	:	
3445.33	He I	3P$_0$-3D	3444.92	−35.68	0.0167	0.0290	36	
3447.63	He I	3P$_0$-3D	3447.10	−46.09	0.185	0.321	12	
3450.26	He I	3P$_0$-3D	3449.75	−44.31	0.0193	0.0334	33	
3453.30	He I	3P$_0$-3D	3452.85	−39.07	0.0242	0.0418	29	
3456.84	He I	3P$_0$-3D	3456.31	−45.96	0.0287	0.0497	27	
3460.99	He I	3P$_0$-3D	3460.51	−41.58	0.0277	0.0478	27	
3465.92	He I	3P$_0$-3D	3465.43	−42.38	0.0383	0.0660	23	
3466.50	[N I]	4S$_0$-2P$_0$	3466.04	−39.78	0.0429	0.0738	21	
3471.80	He I	44	3471.34	−39.72	0.0487	0.0836	20	
3478.97	He I	43	3478.49	−41.36	0.0494	0.0847	20	
3487.73	He I	42	3487.24	−42.12	0.0655	0.112	17	
3498.64	He I	40	3498.15	−41.99	0.0683	0.116	17	
3512.51	He I	38	3512.02	−41.82	0.0963	0.163	15	
3530.50	He I	36	3530.00	−42.46	0.147	0.248	13	
3554.42	He I	34	3553.92	−42.17	0.198	0.332	12	
3562.95	He I	33	3562.49	−38.71	0.0118	0.0198	:	
3568.50	Ne II	5	3568.02	−40.33	0.0262	0.0438	28	
3574.61	Ne II	5	3574.07	−45.29	0.0107	0.0178	:	
3587.28	He I	31	3586.78	−41.79	0.267	0.444	12	
3590.86	C II	23	3590.07	−65.96	0.0178	0.0294	35	
3599.32	He I	30	3598.82	−41.65	0.0182	0.0302	34	
3613.64	He I	6	3613.12	−43.14	0.318	0.524	11	
3634.25	He I	28	3633.73	−42.90	0.381	0.624	11	
3669.47	H I	H25	3668.94	−43.30	0.305	0.495	12	
3671.48	H I	H24	3670.95	−43.28	0.350	0.568	11	
3673.76	H I	H23	3673.24	−42.43	0.401	0.650	11	
3676.37	H I	H22	3675.84	−43.22	0.456	0.739	11	
3679.36	H I	H21	3678.83	−43.18	0.517	0.836	11	
3682.81	H I	H20	3682.28	−43.14	0.575	0.929	11	
3686.83	H I	H19	3686.30	−43.10	0.666	1.075	11	
3691.56	H I	H18	3691.03	−43.04	0.739	1.191	11	
3694.22	Ne II	1	3693.69	−43.01	0.0474	0.0764	20	
3697.15	H I	H17	3696.62	−42.98	0.847	1.364	10	
3703.86	H I	H16	3703.34	−42.09	0.910	1.462	10	
3705.04	He I	25	3704.48	−45.31	0.582	0.935	11	
3709.62	Ne II	1	3709.09	−42.83	0.0227	0.0364	30	
3711.97	H I	H15	3711.48	−39.57	1.172	1.879	10	

Table 2 – *continued*

λ_0 (Å)	Ion	Mult.	λ_{obs}	V_{rad} (km s^{-1})	$F(\lambda)/F(\mathrm{H}ref)^d$	$I(\lambda)/I(\mathrm{H}\beta)^e$	Err (%)^f	Notes
3713.08	Ne II	5	*	*	*	*	*	
3717.72	S III	6	3717.26	−37.09	0.0144	0.0231	:	
3721.83	[S III]	2F	3721.27	−45.11	2.571	4.110	10	
3721.93	H I	H14	*	*	*	*	*	
3726.03	[O II]	1F	3725.33	−56.32	20.54	32.80	10	
3728.82	[O II]	1F	3728.01	−65.12	8.244	13.15	10	
3734.37	H I	H13	3733.81	−44.96	1.520	2.421	10	
3737.55	Ne II	4D-2[2]$_0$	3737.15	−32.08	0.0113	0.0180	:	
3745.94	He I	1P$_0$-1D	3745.39	−44.02	0.0132	0.0210	:	
3750.15	H I	H12	3749.60	−43.97	2.029	3.216	10	
3756.10	He I	66	3755.57	−42.30	0.0158	0.0250	38	
3762.47	O II	4S$_0$-4P	3761.94	−42.23	0.0075	0.0119	:	
3766.26	Ne II	1	3765.78	−38.21	0.0171	0.0270	36	
3768.78	He I	65	3770.08	103.41	2.498	3.935	10	
3770.63	H I	H11	*	*	*	*	*	
3777.14	Ne II	1	3776.67	−37.30	0.0178	0.0280	35	
3784.89	He I	64	3784.31	−45.94	0.0275	0.0431	27	
3797.90	H I	H10	3797.35	−43.42	3.454	5.394	10	
3797.63	[S III]	2F	*	*	*	*	*	
3805.74	He I	63	3805.39	−27.57	0.0620	0.0966	18	
3819.61	He I	22	3819.07	−42.38	1.061	1.646	10	
3829.77	Ne II	39	3829.21	−43.84	0.0134	0.0207	:	
3831.72	C II	96	3831.08	−50.07	0.0310	0.0479	25	
3835.39	H I	H9	3834.83	−43.77	4.891	7.547	10	
3853.66	Si II	1	3853.17	−38.12	0.0070	0.0107	61	
3856.02	Si II	1	3855.47	−42.76	0.0769	0.118	16	
3862.59	Si II	1	3862.07	−40.36	0.0479	0.0732	20	
3868.75	[Ne III]	1F	3868.15	−46.49	43.69	66.67	9	
3880.33	Ar II	54	3879.62	−54.85	0.0310	0.0471	22	
3882.19	O II	12	3881.73	−35.52	0.0172	0.0262	31	
3888.65	He I	2	3888.34	−23.90	11.99	18.17	7	
3889.05	H I	H8	*	*	*	*	*	
	?		3900.55		0.0483	0.0728	17	
3918.98	C II	4	3918.52	−35.19	0.0253	0.0379	25	
3920.68	C II	4	3920.21	−35.94	0.0437	0.0655	18	
3926.53	He I	58	3925.96	−43.52	0.114	0.170	11	
3935.94	He I	57	3935.40	−41.13	0.0061	0.0091	:	
3964.73	He I	5	3964.12	−46.13	0.660	0.973	8	
3967.46	[Ne III]	1F	3966.89	−43.07	13.35	19.66	7	
3970.07	H I	H7	3969.47	−45.31	10.26	15.09	7	
3973.24	O II	6	3972.71	−39.99	0.0150	0.0220	34	
3994.98	N II	12	3994.41	−42.77	0.0327	0.0477	21	
4009.26	He I	55	4008.64	−46.36	0.182	0.264	10	
4023.98	He I	54	4023.40	−43.21	0.0175	0.0252	31	
4026.21	He I	18	4025.60	−45.42	2.108	3.034	7	
4035.07	O II	68	4034.53	−40.12	0.0140	0.0200	36	
4035.08	N II	39a	*	*	*	*	*	
4041.31	N II	39b	4040.71	−44.51	0.0376	0.0538	20	
4043.53	N II	39a	4042.91	−45.97	0.0122	0.0175	39	
4060.60	O II	97	4060.19	−30.27	0.0147	0.0209	35	
4062.94	O II	50	4062.27	−49.44	0.0065	0.0091	:	
4068.60	[S II]	1F	4067.99	−44.95	4.374	6.189	7	
4069.62	O II	10	*	*	*	*	*	
4069.89	O II	10	*	*	*	*	*	
4072.15	O II	10	4071.57	−42.70	0.118	0.167	11	
4075.86	O II	10	4075.68	−49.27	1.600	2.257	7	
4076.35	[S II]	1F	*	*	*	*	*	
4087.15	O II	48	4086.53	−45.48	0.0118	0.0166	:	
4089.29	O II	48	4088.64	−47.65	0.0577	0.0809	16	*a*
4092.93	O II	10	4092.33	−43.95	0.0132	0.0185	38	
4097.26	O II	48	4096.69	−41.71	0.204	0.285	9	
4101.74	H I	H6	4101.12	−45.32	17.43	24.33	7	
4110.79	O II	20	4110.10	−50.32	0.0211	0.0293	27	
4119.22	O II	20	4118.59	−45.85	0.0376	0.0521	20	

Table 2 – *continued*

λ_0 (Å)	Ion	Mult.	λ_{obs}	V_{rad} (km s^{-1})	$F(\lambda)/F(\mathrm{H}ref)^d$	$I(\lambda)/I(\mathrm{H}\beta)^e$	Err (%)^f	Notes
4120.82	He I	16	4120.20	−45.11	0.287	0.397	8	a
4129.32	O II	19	4128.73	−42.83	0.0069	0.0095	:	
4132.80	O II	19	4132.12	−49.33	0.0426	0.0587	18	
4143.76	He I	53	4143.13	−45.58	0.308	0.422	9	
4145.90	O II	106	4145.43	−33.99	0.0207	0.0283	28	
4146.08	O II	106	*	*	*	*	*	
4153.30	O II	19	4152.65	−46.92	0.0524	0.0715	16	
4156.53	O II	19	4155.96	−41.11	0.0720	0.0982	14	a
4168.97	He I	52	4168.42	−39.55	0.0471	0.0639	17	
4171.61	N II	43a	4170.99	−44.56	0.0035	0.0047	:	
4176.16	N II	43a	4175.56	−43.07	0.0091	0.0123	:	
4185.45	O II	36	4184.82	−45.13	0.0313	0.0422	22	
4189.79	O II	36	4189.17	−44.36	0.0456	0.0613	18	
4219.76	Ne II	52a	4219.12	−45.47	0.0117	0.0156	:	
4231.53	Ne II	52b	4230.94	−41.80	0.0098	0.0129	:	
4233.27	Ni II	2G$_0$-2F	4232.51	−53.82	0.0250	0.0329	25	
4236.91	N II	48	4236.41	−35.38	0.0313	0.0412	22	
4237.05	N II	48	*	*	*	*	*	
4241.78	N II	48	4241.15	−44.53	0.0313	0.0410	22	
4243.97	[Fe II]	21F	4243.40	−40.26	0.0112	0.0147	:	
4254.00	O II	101	4253.21	−55.67	0.0332	0.0434	21	
4267.15	C II	6	4266.43	−50.58	0.551	0.715	8	
4275.55	O II	67	4275.69	9.82	0.0905	0.117	12	
4276.75	O II	67	*	*	*	*	*	a
4281.32	O II	53b	4280.75	−39.91	0.0058	0.0075	:	
4282.96	O II	67c	4282.57	−27.30	0.0118	0.0152	:	
4285.69	O II	78	4284.91	−54.56	0.0098	0.0126	:	
4287.39	[Fe II]	7F	4286.80	−41.26	0.0128	0.0164	38	
4291.25	O II	55	4290.58	−46.81	0.0058	0.0074	:	
4292.21	O II	78	4291.58	−44.00	0.0063	0.0080	:	
4294.92	O II	54	4294.15	−53.75	0.0157	0.0201	33	
4303.61	O II	65	4303.14	−32.74	0.0226	0.0288	27	
4303.82	O II	53	*	*	*	*	*	
4307.23	O II	54	4306.61	−43.15	0.0044	0.0056	:	
4309.00	O II	4D-D[1]$_0$	4308.39	−42.44	0.0041	0.0052	:	
4309.01	O II	4D-D[1]$_0$	*	*	*	*	*	
4317.14	O II	2	4316.51	−43.75	0.0338	0.0428	21	a
4319.63	O II	2	4319.00	−43.72	0.0241	0.0306	25	
4325.76	O II	2	4325.19	−39.50	0.0192	0.0242	30	
	?		*	*	*	*	*	
4329.75	C II	2D-2F$_0$	4329.14	−41.54	0.0027	0.0033	:	
4332.71	O II	65	4332.13	−40.13	0.0063	0.0079	:	
4336.83	O II	2	4336.12	−49.08	0.0128	0.0161	37	
4340.47	H I	H5	4339.81	−45.59	37.71	47.33	7	
4345.56	O II	2	4344.94	−42.08	0.0456	0.0571	18	
4346.85	[Fe II]	21F	4346.77	−5.52	0.0059	0.0074	:	
4349.43	O II	2	4348.77	−45.49	0.0732	0.0914	14	
4359.34	[Fe II]	7F	4358.61	−50.20	0.0120	0.0150	39	
4363.21	[O III]	2F	4362.58	−43.29	3.045	3.783	7	
4366.89	O II	2	4366.21	−46.68	0.0532	0.0659	16	
4368.19	O I	5	4367.64	−37.75	0.0581	0.0720	15	
4368.25	O I	5	*	*	*	*	*	
4371.59	C II	45	4371.26	−22.63	0.0118	0.0146	40	
4379.55	Ne II	60	4378.97	−39.70	0.0072	0.0089	:	
4387.93	He I	51	4387.26	−45.78	0.630	0.773	8	
4391.94	Ne II	55e	4391.61	−22.53	0.0400	0.0490	19	a
4409.30	Ne II	55e	4408.67	−42.83	0.0194	0.0236	29	
4414.90	O II	5	4414.27	−42.78	0.0331	0.0402	22	
4416.76	Ne II	2D-2[2]$_0$	4416.21	−37.33	0.0437	0.0530	18	
4416.97	O II	5	*	*	*	*	*	
4428.54	Ne II	57	4427.75	−53.48	0.0179	0.0215	31	
4430.94	Ne II	61	4430.28	−44.65	0.0056	0.0067	:	
4432.74	N II	55a	4432.14	−40.58	0.0331	0.0398	21	
4437.55	He I	50	4436.89	−44.59	0.0626	0.0752	15	

Table 2 – *continued*

λ_0 (Å)	Ion	Mult.	λ_{obs}	V_{rad} (km s^{-1})	$F(\lambda)/F(\mathrm{H}ref)^d$	$I(\lambda)/I(\mathrm{H}\beta)^e$	Err (%)^f	Notes
4439.46	Ar II	2D$_0$-2D	4438.78	−45.92	0.0061	0.0074	:	
4439.88	Ar II	2D$_0$-2D	*	*	*	*	*	
4442.69	Ne II	60	4441.83	−58.03	0.0120	0.0144	39	
4447.03	N II	1P-1D$_0$	4446.28	−50.56	0.0053	0.0063	:	
4448.46	Ar II	2D$_0$-2D	4447.86	−40.44	0.0088	0.0105	:	
4448.88	Ar II	2D$_0$-2D	*	*	*	*	:	
4452.38	O II	5	4451.59	−53.19	0.0127	0.0152	38	
4457.05	Ne II	2D-2[2]$_0$	4456.75	−20.18	0.0121	0.0144	39	
4457.26	Ne II	2D-2[2]$_0$	*	*	*	*	*	
	?		4461.27		0.0038	0.0045	:	?
4463.65	O I	3P-3P$_0$	4462.84	−54.40	0.0051	0.0061	:	
4463.66	O I	3P-3P$_0$	*	*	*	*	*	
4465.41	O II	94	4464.76	−43.64	0.0196	0.0232	29	
4467.92	O II	94	4467.21	−47.64	0.0088	0.0104	:	
4471.47	He I	14	4470.83	−42.91	5.317	6.286	7	
4481.21	Mg II	4	4480.74	−31.44	0.0316	0.0372	22	
4483.43	S II	4D$_0$-4P	4482.71	−48.14	0.0032	0.0038	:	
4491.23	O II	86a	4490.57	−44.06	0.0161	0.0189	33	
4498.92	Ne II	4P-2[1]$_0$	4498.41	−33.98	0.0083	0.0096	:	
4499.12	Ne II	4P-2[1]$_0$	*	*	*	*	*	
4520.69	Si II	2D-2P$_0$	4520.05	−42.44	0.0182	0.0211	30	
4525.76	Ne I	–	4524.90	−56.97	0.0081	0.0094	:	
4530.41	N II	58b	4529.43	−64.85	0.0524	0.0603	16	
4530.86	N III	3	*	*	*	*	*	
4552.52	N II	58a	4552.05	−30.95	0.0203	0.0231	29	
4562.60	Mg I]	1	4561.72	−57.82	0.0134	0.0152	37	
4571.10	Mg I]	1	4570.36	−48.53	0.217	0.246	9	a
4590.97	O II	15	4590.30	−43.75	0.0532	0.0596	16	
4595.95	O II	15	4595.47	−31.31	0.0449	0.0502	18	
4596.18	O II	15	*	*	*	*	*	
4601.48	N II	5	4600.92	−36.48	0.0543	0.0606	16	
4607.13	[Fe III]	3F	4606.42	−46.20	0.0367	0.0408	20	
4609.44	O II	92a	4609.17	−17.56	0.0547	0.0608	16	
4610.20	O II	2D-F[2]$_0$	*	*	*	*	*	
4621.39	N II	5	4620.68	−46.06	0.0242	0.0268	26	
4630.54	N II	5	4629.82	−46.61	0.132	0.145	11	
4634.14	N III	2	4633.46	−43.99	0.110	0.121	11	
4638.86	O II	1	4638.17	−44.59	0.0920	0.101	12	
4640.64	N III	2	4639.94	−45.22	0.210	0.230	9	
4641.81	O II	1	4641.11	−45.21	0.202	0.221	9	
4643.06	N II	5	4642.29	−49.72	0.0622	0.0681	15	
4649.13	O II	1	4648.44	−44.49	0.367	0.400	8	
4650.84	O II	1	4650.13	−45.77	0.0845	0.0922	13	
4658.05	[Fe III]	3F	4657.32	−46.98	0.227	0.247	9	
4661.63	O II	1	4660.92	−45.66	0.0973	0.106	12	a
4673.73	O II	1	4672.97	−48.75	0.0124	0.0134	39	
4676.24	O II	1	4675.54	−44.88	0.0554	0.0598	17	
4699.22	O II	25	4698.51	−45.30	0.0214	0.0229	28	
4701.62	[Fe III]	3F	4700.80	−52.29	0.0743	0.0793	14	
4705.35	O II	25	4704.67	−43.32	0.0119	0.0127	:	
4711.37	[Ar IV]	1F	4710.94	−27.36	0.0634	0.0674	12	
4713.14	He I	12	4712.47	−42.62	0.698	0.741	8	
4733.93	[Fe III]	3F	4733.13	−50.66	0.0152	0.0160	34	
4740.17	[Ar IV]	1F	4739.56	−38.58	0.218	0.229	9	
4754.69	[Fe III]	3F	4753.98	−44.77	0.0176	0.0183	31	
4769.43	[Fe III]	3F	4768.67	−47.77	0.0184	0.0191	30	
4777.68	[Fe III]	3F	4776.93	−47.06	0.0101	0.0105	:	
4788.13	N II	20	4787.42	−44.45	0.0148	0.0152	34	
4802.70	C II	17.08	4802.51	−11.86	0.0221	0.0226	27	
4814.55	[Fe II]	20F	4813.89	−41.10	0.0080	0.0081	:	
4815.51	S II	9	4814.85	−41.09	0.0071	0.0072	:	
4861.33	H I	H4	4860.59	−45.63	100.0	100.0	7	
4881.00	[Fe III]	2F	4880.21	−48.52	0.128	0.127	11	
4921.93	He I	48	4921.19	−45.07	1.701	1.662	7	

Table 2 – *continued*

λ_0 (Å)	Ion	Mult.	λ_{obs}	V_{rad} (km s^{-1})	$F(\lambda)/F(\mathrm{H}ref)^d$	$I(\lambda)/I(\mathrm{H}\beta)^e$	Err (%)^f	Notes
4931.32	[O III]	1F	4930.49	−50.46	0.100	0.0977	12	
4958.91	[O III]	1F	4958.17	−44.74	292.2	281.6	6	
4980.05	O I	3P-3S$_0$	4979.30	−47.56	0.0108	0.0103	19	
4987.20	[Fe III]	2F	4986.62	−34.87	0.0335	0.0319	11	
4987.38	N II	24	*	*	*	*	*	
4994.37	N II	24	4993.68	−41.42	0.0757	0.0720	8	
5006.84	[O III]	1F	5006.09	−44.91	892.8	845.5	6	
5015.68	He I	4	5014.89	−47.22	3.195	3.016	6	
5025.66	N II	19	5025.00	−39.37	0.0102	0.0096	20	
5032.13	C II	2P-2D	5031.29	−50.04	0.0614	0.0576	9	
5035.94	C II	2P-2D	5035.07	−51.79	0.0380	0.0356	10	
5041.03	Si II	5	5040.29	−44.01	0.178	0.167	8	
5045.10	N II	4	5044.44	−39.22	0.0678	0.0633	9	
5048.18	[Fe II]	a2P-c2D	5047.34	−49.88	0.641	0.598	7	
5055.98	Si II	5	5055.39	−34.98	0.110	0.103	8	
5121.82	C II	12	5121.09	−42.73	0.0177	0.0161	14	
5145.16	C II	4P$_0$-4P	5144.38	−45.45	0.0033	0.0030	:	
5146.61	O I	28	5145.97	−37.28	0.0099	0.0089	20	
5146.65	O I	28	*	*	*	*	*	
5158.00	[Fe II]	18F	5157.11	−51.73	0.0097	0.0087	20	
5158.81	[Fe II]	19F	5158.05	−44.17	0.0318	0.0286	11	
	?		5172.58		0.0056	0.005	28	
5175.89	N II	5D$_0$-5F	5175.23	−38.23	0.0106	0.0095	19	
5179.52	N II	5D$_0$-5F	5178.84	−38.20	0.0274	0.0245	12	
5191.82	[Ar III]	3F	5191.00	−47.35	0.147	0.131	8	
5197.90	[N I]	1F	5197.10	−46.14	0.555	0.493	7	
5200.06	[Fe II]	19F	5199.43	−36.32	0.365	0.324	7	
5200.26	[N I]	1F	*	*	*	*	*	
5261.61	[Fe II]	19F	5260.92	−39.31	0.0173	0.0151	15	
5270.40	[Fe III]	1F	5269.71	−39.25	0.104	0.0906	8	
5274.97	O I	27	5274.40	−32.39	0.0064	0.0055	26	
5275.12	O I	27	*	*	*	*	*	
5298.89	O I	26	5298.33	−31.68	0.0256	0.0220	12	
5299.04	O I	26	*	*	*	*	*	
5333.65	[Fe II]	19F	5332.95	−39.35	0.0090	0.0077	21	
5342.38	C II	17.06	5341.61	−43.21	0.0414	0.0352	10	
5346.02	[Kr IV]	4S-2D	5345.27	−42.06	0.0096	0.0081	20	
	?		5358.44		0.0103	0.0087	19	
	?		*		*	*	*	
5367.73	C II	4P$_0$-4D	5367.22	−28.48	0.0062	0.0052	27	
5370.39	C II	4P$_0$-4D	5369.57	−45.78	0.0055	0.0046	29	
5376.45	[Fe II]	19F	5375.81	−35.69	0.0170	0.0143	15	
5405.15	Ne II	2[5]$_0$-2[6]	5404.49	−36.61	0.0061	0.0051	27	?
5412.00	[Fe III]	1F	5411.13	−48.19	0.0207	0.0173	13	
5433.13	[Fe II]	18F	5432.16	−53.52	0.0115	0.0096	19	
5452.07	N II	29	5451.32	−41.24	0.0121	0.0100	18	
5454.22	N II	29	5453.33	−48.92	0.0289	0.0238	12	
5462.58	N II	29	5461.90	−37.32	0.0231	0.0189	13	
5478.09	N II	29	5477.30	−43.23	0.0069	0.0056	25	
5480.05	N II	29	5479.22	−45.41	0.0142	0.0116	16	
5495.98	N II	29	5494.90	−58.91	0.0382	0.0311	10	
5506.87	[Cr III]	2F	5506.09	−42.46	0.0034	0.0027	:	?
5512.77	O I	25	5511.98	−42.96	0.0113	0.0092	19	
5517.71	[Cl III]	1F	5516.91	−43.47	0.395	0.320	7	
5526.23	N II	63	5525.49	−40.14	0.0094	0.0076	21	
5527.34	[Fe II]	17F	5526.56	−42.31	0.0145	0.0118	16	
5530.24	N II	63	5529.49	−40.66	0.0165	0.0133	15	
5535.36	N II	63	5534.59	−41.70	0.0335	0.0270	11	
5537.88	[Cl III]	1F	5537.06	−44.39	1.151	0.928	7	
5543.47	N II	63	5542.71	−41.10	0.0112	0.0090	19	
5551.96	N II	63	5551.20	−41.04	0.0130	0.0104	17	?
5577.34	[O I]	3F	5576.61	−39.24	0.0589	0.0470	9	
5640.19	S II	4F-4D$_0$	5639.30	−47.31	0.0087	0.0068	22	
5666.64	N II	3	5665.84	−42.32	0.1371	0.107	8	

Table 2 – *continued*

λ_0 (Å)	Ion	Mult.	λ_{obs}	V_{rad} (km s^{-1})	$F(\lambda)/F(\mathrm{H}ref)^d$	$I(\lambda)/I(\mathrm{H}\beta)^e$	Err (%)^f	Notes
5676.02	N II	3	5675.22	−42.25	0.0495	0.0386	10	
5679.56	N II	3	5678.78	−41.17	0.244	0.190	7	
5686.21	N II	3	5685.43	−41.12	0.0321	0.0250	11	
5710.76	N II	3	5709.97	−41.47	0.0414	0.0320	10	
5730.65	N II	3	5729.79	−44.99	0.0032	0.0025	:	
5739.73	Si III	4	5739.02	−37.08	0.0074	0.0057	24	
5747.33	O II	2D$_0$-2F	5746.52	−42.25	0.0107	0.0082	19	
5754.64	[N II]	3F	5753.79	−44.28	6.074	4.648	7	
5867.74	[Kr IV]	4S-2D	5867.02	−36.79	0.0252	0.0188	12	
5875.60	He I	11	5874.83	−39.29	26.75	19.93	7	
6151.43	C II	16.04	6150.41	−49.71	0.0385	0.0271	10	
6300.30	[O I]	1F	6299.38	−43.78	7.740	5.289	7	b
6312.10	[S III]	3F	6311.20	−42.75	4.930	3.361	7	
6340.58	N II	3D$_0$-3P	6339.64	−44.44	0.0044	0.0030	34	
6347.11	Si II	2	6346.21	−42.51	0.151	0.102	8	
6363.78	[O I]	1F	6362.85	−43.81	2.692	1.817	7	b
6371.36	Si II	2	6370.49	−40.94	0.110	0.0741	8	
6402.25	Ne I	1	6401.33	−43.08	0.0160	0.0107	15	
6461.95	C II	17.04	6460.86	−50.57	0.0993	0.0658	8	
6482.05	N II	1P$_0$-1P	6481.18	−40.24	0.0291	0.0192	11	
6486.46	O II	G[3]$_0$-1[4]	6485.51	−43.91	0.0029	0.0019	:	
6527.24	[N II]	1F	6526.25	−39.04	0.0468	0.0306	10	
6548.03	[N II]	1F	6546.95	−49.45	87.42	56.95	6	
6555.56	[Br III]	–	6554.99	−26.07	0.0149	0.0097	:	?
6562.82	H I	H3	6561.74	−49.33	436.9	283.8	6	
6578.05	C II	2	6576.93	−51.04	0.464	0.301	6	
6583.41	[N II]	1F	6582.32	−49.64	275.7	178.4	6	
6610.56	N II	31F	6609.65	−41.27	0.0088	0.0056	22	
6641.03	O II	43a	6640.36	−30.25	0.0078	0.0050	24	
6678.15	He I	46	6677.21	−42.20	8.195	5.206	7	
6716.47	[S II]	2F	6715.37	−49.10	7.088	4.470	10	
6730.85	[S II]	2F	6729.76	−48.55	14.32	9.004	10	
6779.93	C II	14	6780.47	23.88	1.779	0.111	11	
6780.59	C II	14	*	*	*	*	*	
6791.47	C II	14	6790.49	−43.26	0.104	0.0065	30	
6803.01	[Cr II]	b4D-c2F	6802.24	−33.93	0.805	0.0503	12	?
6809.99	N II	54	6808.98	−44.46	0.0853	0.0053	34	
6826.70	[Kr III]	3P-1D	6826.27	−18.88	0.344	0.0215	16	
6827.88	He I	1/16	*	*	*	*	*	
6855.88	He I	1/15	6856.06	7.87	0.511	0.0319	14	a
6933.89	He I	1/13	6932.98	−39.34	0.151	0.0094	24	
6989.47	He I	1/12	6988.46	−43.32	0.161	0.0100	23	
7001.92	O I	21	7001.14	−33.40	0.883	0.0547	12	
7062.26	He I	1/11	7064.24	84.05	136.2	8.411	10	
7065.28	He I	10	*	*	*	*	*	
7135.78	[Ar III]	1F	7134.76	−42.85	500.6	30.81	10	
	?		7152.71		0.161	0.0099	16	
7155.16	[Fe II]	14F	7154.16	−41.90	1.946	0.120	11	
7160.61	He I	1/10	7159.52	−45.63	0.340	0.0210	16	
7231.34	C II	3	7230.08	−52.24	2.514	0.154	11	
7236.42	C II	3	7235.36	−43.91	3.823	0.234	11	c
7237.17	C II	3	*	*	*	*	*	
7254.15	O I	3P-3S$_0$	7253.36	−32.81	1.576	0.0965	11	b
7254.45	O I	3P-3S$_0$	*		*	*	*	
7254.53	O I	3P-3S$_0$	*		*	*	*	
7281.35	He I	45	7280.29	−43.64	13.81	0.845	10	
7298.05	He I	1/9	7296.91	−46.83	0.610	0.0373	13	
7318.92	[O II]	2F	7318.81	−4.51	119.3	7.284	10	b
7319.99	[O II]	2F	*		*	*	*	
7329.66	[O II]	2F	7329.12	−22.09	107.7	6.572	10	b
7330.73	[O II]	2F	*		*	*	*	
7377.83	[Ni II]	2F	7376.86	−39.42	0.991	0.0603	12	
7388.16	[Fe II]	14F	7387.04	−45.45	0.218	0.0132	20	
7423.64	N I	3	7422.56	−43.61	0.139	0.0085	25	

Table 2 – *continued*

λ_0 (Å)	Ion	Mult.	λ_{obs}	V_{rad} (km s^{-1})	$F(\lambda)/F(\mathrm{H}ref)^d$	$I(\lambda)/I(\mathrm{H}\beta)^e$	Err (%)^f	Notes
7442.30	N I	3	7441.28	−41.09	0.262	0.0159	18	
7452.54	[Fe II]	14F	7451.17	−55.11	0.439	0.0267	15	
	?		*	*	*	*	*	
7468.31	N I	3	7467.26	−42.15	0.501	0.0304	14	
7499.85	He I	1/8	7498.73	−44.77	0.822	0.0498	12	
7504.96	O II	2G-G[5]$_0$	7503.85	−44.34	0.121	0.0073	28	
7509.24	N II	3P-1P	7508.46	−31.14	0.0511	0.0031	:	
7519.49	C II	16.08	7518.55	−37.48	0.152	0.0092	24	
7519.86	C II	16.08	*	*	*	*	*	
7530.54	[Cl IV]	1F	7529.42	−44.59	0.627	0.0379	13	
7535.40	[Xe IV]	4S-2D	7534.05	−53.71	0.0526	0.0032	:	?
7561.27	[Fe II]	b4F-b2D	7560.30	−38.46	0.0454	0.0027	:	?
7751.10	[Ar III]	2F	7750.00	−42.55	126.5	7.577	10	
7771.93	O I	1	7770.83	−42.43	0.283	0.0169	18	*b*
7816.13	He I	1/7	7814.98	−44.11	1.335	0.0797	11	
7875.99	[P II]	1D-1S	7874.79	−45.68	0.275	0.0164	18	?
8045.63	[Cl IV]	1F	8044.64	−36.89	1.261	0.0746	12	
8057.59	He I	4/18	8056.32	−47.25	0.168	0.0099	23	
8084.29	He I	4/17	8083.05	−45.98	0.134	0.0079	26	
8094.08	He I	2/10	8093.10	−36.30	0.158	0.0093	24	
8116.30	He I	4/16	8115.30	−36.94	0.173	0.0102	22	
8125.30	[Cr II]	1F	8124.29	−37.27	0.0782	0.0046	36	?
8203.85	He I	4/14	8202.66	−43.49	0.266	0.0156	18	
8216.34	N I	2	8215.04	−47.43	0.695	0.0408	13	
8223.14	N I	2	8222.01	−41.20	0.579	0.0340	14	*c*
8267.94	H I	P34	8266.69	−45.32	1.147	0.0672	12	
8271.93	H I	P33	8270.67	−45.67	1.352	0.0792	12	
8276.31	H I	P32	8275.26	−38.03	0.991	0.0581	12	*c*
8286.43	H I	P30	8285.23	−43.41	1.747	0.102	11	
8292.31	H I	P29	8291.12	−43.02	1.867	0.109	11	
8298.83	H I	P28	8297.57	−45.52	2.324	0.136	11	
8306.11	H I	P27	8304.84	−45.84	1.920	0.112	11	*c*
8314.26	H I	P26	8313.04	−43.99	2.514	0.147	11	*c*
8323.42	H I	P25	8322.34	−38.90	2.281	0.133	11	*c*
8329.87	He I	6/23	8328.74	−40.67	0.161	0.0094	23	
8333.78	H I	P24	8332.55	−44.25	3.485	0.204	11	
8343.27	He I	6/22	8344.30	37.01	4.774	0.279	11	*b*
8345.55	H I	P23	*	*	*	*	*	
8359.00	H I	P22	8357.80	−43.04	4.140	0.242	11	*c*
8361.71	He I	68	8360.49	−43.74	2.218	0.130	11	
8374.48	H I	P21	8373.28	−42.96	5.112	0.299	10	
8392.40	H I	P20	8391.15	−44.65	5.218	0.304	11	
8397.41	He I	6/19	8396.16	−44.63	0.128	0.0075	27	
8413.32	H I	P19	8412.08	−44.19	6.063	0.354	11	
8421.96	He I	6/18	8420.81	−40.94	0.222	0.0129	20	
8433.85	[Cl III]	3F	8432.47	−49.05	0.438	0.0255	15	
8437.96	H I	P18	8436.72	−44.06	6.253	0.364	11	
8446.25	O I	4	8445.31	−33.36	15.48	0.902	10	
8446.36	O I	4	*	*	*	*	*	
8446.76	O I	4	*	*	*	*	*	
8451.16	He I	6/17	8449.96	−36.89	0.171	0.0010	23	
8453.61	He I	7/17	*	*	*	*	*	
8480.90	[Cl III]	3F	8479.63	−44.89	0.547	0.0318	14	
8486.27	He I	6/16	8485.01	−44.51	0.357	0.0208	16	
8499.70	[Cl III]	3F	8501.15	51.14	9.632	0.560	10	
8502.48	H I	P16	*	*	*	*	*	
8528.99	He I	6/15	8527.78	−42.53	0.429	0.0249	15	
8531.51	He I	7/15	8530.20	−46.17	0.0699	0.0041	38	
8648.27	He I	6/13	8647.04	−42.64	0.525	0.0304	14	*b*
8650.83	He I	7/13	8649.76	−37.08	0.262	0.0151	18	*b*
8665.02	H I	P13	8663.77	−43.25	13.81	0.799	10	*b*
8680.28	N I	1	8679.06	−42.14	0.408	0.0236	15	
8683.40	N I	1	8682.19	−41.77	0.463	0.0267	15	*b*
8686.15	N I	1	8684.96	−41.07	0.389	0.0225	16	

Table 2 – *continued*

λ_0 (Å)	Ion	Mult.	$\lambda_{\rm obs}$	$V_{\rm rad}$ (km s^{-1})	$F(\lambda)/F({\rm H}ref)^d$	$I(\lambda)/I({\rm H}\beta)^e$	Err (%)^f	Notes
8703.25	N I	1	8701.99	−43.40	0.224	0.0129	20	
8711.70	N I	1	8710.48	−41.98	0.325	0.0188	17	
8718.84	N I	1	8717.61	−41.95	0.149	0.0086	25	
8727.13	[C I]	3F	8725.83	−44.66	0.934	0.0539	12	
8728.90	N I	1	*	*	*	*	*	
8733.43	He I	6/12	8732.16	−43.60	0.731	0.0422	13	
8736.04	He I	7/12	8734.69	−46.33	0.230	0.0133	19	
8740.10	He I	5/12	8738.91	−40.82	0.0475	0.0027	:	
8750.47	H I	P12	8749.19	−43.85	19.18	1.106	10	
8776.60	He I	4/9	8775.60	−34.16	1.134	0.0654	12	b
8816.50	He I	10/12	8815.35	−39.10	0.0957	0.0055	31	
8829.40	[S III]	1F	8827.67	−58.74	1.265	0.0728	12	b
8845.38	He I	6/11	8844.06	−44.74	1.083	0.0623	12	
8848.05	He I	7/11	8846.77	−43.37	0.589	0.0339	14	b
8854.20	He I	5/11	8852.74	−49.43	0.180	0.0103	25	
8855.28	[Se III]	3P-1D	*	*	*	*	*	
8862.79	H I	P11	8861.49	−43.97	24.29	1.396	10	
8873.40	C II	2D-2F$_0$	8872.10	−43.92	0.0454	0.0026	:	?
8891.91	[Fe II]	13F	8890.58	−44.84	0.663	0.0381	12	b
8996.99	He I	6/10	8995.66	−44.32	1.472	0.0843	12	
8999.40	He I	7/10	8998.34	−35.31	0.501	0.0287	14	
9014.91	H I	P10	9013.63	−42.57	29.78	1.705	11	c
9063.29	He I	4/8	9061.94	−44.65	1.380	0.0789	9	
9068.60	[S III]	1F	9067.45	−38.02	1145.4	65.49	8	c
9085.42	He I	10/10	9084.05	−45.21	0.264	0.0151	19	
9123.60	[Cl II]	1F	9122.24	−44.69	1.918	0.110	11	
9210.28	He I	6/9	9209.03	−40.69	1.850	0.105	11	
9213.20	He I	7/9	9211.81	−45.23	0.708	0.0403	13	
9229.01	H I	P9	9227.67	−43.53	44.15	2.515	10	b
9516.57	He I	4/7	9515.35	−38.43	1.272	0.0720	12	
9530.60	[S III]	1F	9529.68	−28.94	1467.4	83.02	8	c
9603.44	He I	2/6	9602.12	−41.21	0.4626	0.0261	15	
9824.13	[C I]	3P-1D	9822.00	−65.00	2.619	0.147	11	
9850.26	[C I]	3P-1D	9848.20	−62.70	7.668	0.431	11	b
9902.30	[Kr III]	3P-1D	9901.82	−14.53	3.057	0.172	11	c
9903.46	C II	17.02	*	*	*	*	*	
9982.46	O II	G[5]$_0$-2[6]	9981.00	−43.55	0.247	0.0139	19	
9988.54	O II	G[5]$_0$-2[6]	9988.68	4.20	0.705	0.0396	13	
9990.08	O II	D[3]$_0$-0[4]	*	*	*	*	*	
9991.48	O II	D[3]$_0$-0[4]	*	*	*	*	*	
10008.87	O II	G[4]$_0$-1[5]	10007.46	−43.13	0.144	0.0081	25	
10027.70	He I	6/7	10026.12	−47.24	7.034	0.394	10	b
10031.20	He I	7/7	10029.66	−46.02	1.853	0.104	11	
10049.40	H I	P7	10047.92	−44.15	100.0	5.600	10	
10072.07	He I	5/7	10070.70	−40.84	0.450	0.0252	14	
	?		*		*	*	*	*
10138.40	He I	10/7	10137.04	−40.22	0.524	0.0293	14	
10286.70	[S II]	3F	10285.43	−37.01	31.05	1.732	10	b
10310.70	He I	4/6	10309.85	−24.71	2.640	0.147	11	b
10320.50	[S II]	3F	10318.90	−46.48	32.32	1.801	10	
10336.40	[S II]	3F	10334.83	−45.54	24.93	1.389	10	
10370.50	[S II]	3F	10368.88	−46.83	10.54	0.587	11	
10397.50	[N I]	3F	10396.38	−32.29	8.154	0.454	11	b
10407.40	[N I]	3F	10405.86	−44.36	4.351	0.242	11	

Notes. ^{a}Affected by charge transfer.

^{b}Affected by telluric emission.

^{c}Affected by atmospheric absorption bands.

^{d}Normalized to H β until [S II] 6730 Å line. Normalized to P7 10 047 Å from C II 6780 Å to [N I] 10 407 Å.

^{e}Where I is the reddened corrected flux, with $c({\rm H}\beta) = 0.63$, in units of $100.00 = 1.032 \times 10^{-11}$ erg cm^{-2} s^{-1}.

^{f}Colons indicates errors larger than 40 per cent.

Table 3. Observed and reddening corrected line ratios [$F(H\beta) = 100$] and line identifications in the FIRE spectrum of NGC 5315.

λ_0 (Å)	Ion	Mult.	λ_{obs}	V_{rad} (km s^{-1})	$F(\lambda)/F(Href)^d$	$I(\lambda)/I(H\beta)^e$	Err (%)^f	Notes
8316.55	H I	P26	8315.52	−37.07	2.772	0.162	10	
8325.71	H I	P25	8324.70	−36.32	3.815	0.223	9	
8336.07	H I	P24	8335.18	−31.99	3.937	0.230	9	
8347.84	H I	P23	8346.82	−36.95	5.362	0.313	8	
8361.30	H I	P22	8361.31	0.27	7.923	0.463	8	
8364.04	He I	68	*	*	*	*	*	
8376.78	H I	P21	8376.25	−19.13	6.377	0.372	8	
8394.71	H I	P20	8394.08	−22.55	5.749	0.335	8	
8399.71	He I	6/19	8401.55	65.67	0.378	0.0220	:	
8402.13	He I	7/19	*	*	*	*	*	
8415.63	H I	P19	8415.01	−22.05	6.473	0.377	8	
8424.28	He I	6/18	8423.44	−29.80	0.363	0.0211	30	
8440.28	H I	P18	8439.80	−17.15	6.498	0.379	8	
8448.57	O I	4	8448.28	−10.33	11.02	0.642	7	
8448.68	O I	4	*	*	*	*	*	
8449.08	O I	4	*	*	*	*	*	
8453.48	He I	6/17	8453.54	2.13	0.271	0.0158	:	
8455.93	He I	7/17	*	*	*	*	*	
8469.58	H I	P17	8468.99	−20.80	8.952	0.521	8	
8483.53	[Cl III]	3F	8482.63	−31.82	0.789	0.0459	19	
8488.60	He I	6/16	8488.16	−15.57	0.676	0.0393	22	
8502.50	[Cl III]	3F	8504.11	56.73	10.59	0.615	8	
8504.82	H I	P16	*	*	*	*	*	
8531.38	He I	6/15	8531.54	5.80	0.870	0.0505	19	
8533.87	He I	7/15	*	*	*	*	*	
8547.73	H I	P15	8547.15	−20.27	11.39	0.661	7	
8581.05	[Cl II]	1F	8580.46	−20.61	5.990	0.347	8	
8584.22	He I	6/14	8584.73	17.80	1.246	0.0722	15	
8586.74	He I	7/14	*	*	*	*	*	
8600.75	H I	P14	8600.17	−20.40	12.09	0.701	7	
8619.32	[Fe II]	13F	8618.13	−41.33	2.133	0.123	11	
8650.64	He I	6/13	8650.17	−16.32	0.937	0.0542	18	
8653.20	He I	7/13	*	*	*	*	*	
8667.40	H I	P13	8666.87	−18.16	15.47	0.895	7	
8735.83	He I	6/12	8735.30	−18.04	1.242	0.0716	15	
8738.44	He I	7/12	*	*	*	*	*	
8752.87	H I	P12	8752.47	−13.85	20.14	1.161	7	
8779.34	He I	4/9	8778.77	−19.63	1.340	0.0772	14	
8831.82	[S III]	1F	8830.69	−38.58	0.717	0.0413	21	
8847.83	He I	6/11	8847.00	−28.12	1.171	0.0673	15	
8850.47	He I	7/11	8849.73	−24.96	0.689	0.0396	21	
8856.63	He I	5/11	8855.77	−29.11	0.191	0.0110	:	
8857.71	[Se III]	3P-1D	*	*	*	*	*	
8865.22	H I	P11	8864.77	−15.48	21.11	1.213	7	
8894.37	[Fe II]	13F	8893.71	−21.56	0.398	0.0228	30	
8999.26	He I	6/10	8999.22	−1.33	2.404	0.138	10	
9002.21	He I	7/10	*	*	*	*	*	
9017.38	H I	P10	9016.76	−20.91	32.13	1.839	6	
9071.09	[S III]	1F	9070.84	−8.18	1029	58.82	6	
9126.10	[Cl II]	1F	9125.24	−28.36	2.126	0.121	11	
9212.85	He I	6/9	9212.09	−24.80	2.815	0.160	10	
9215.76	He I	7/9	9214.90	−28.04	0.830	0.0473	19	
9231.54	H I	P9	9231.02	−16.85	43.96	2.503	6	
9466.17	He I	1/5	9464.99	−37.38	6.913	0.392	7	
9519.44	He I	4/7	9518.95	−15.49	6.077	0.344	7	
9533.21	[S III]	1F	9532.80	−13.10	2848	161.1	6	
9548.59	H I	P8	9547.93	−20.65	68.41	3.869	6	
9606.07	He I	2/6	9604.93	−35.83	0.590	0.0333	23	
9628.34	He I	1P$_0$-1D	9627.71	−19.50	0.642	0.0362	22	
9826.82	[C I]	3P-1D	9826.04	−24.01	1.753	0.0886	12	
9852.96	[C I]	3P-1D	9852.25	−21.61	4.796	0.270	7	
9905.00	[Kr III]	3P-1D	9905.53	15.95	3.613	0.203	8	
9906.18	C II	17.02	*	*	*	*	*	
9985.19	O II	G[5]$_0$-2[6]	9984.70	−14.56	0.321	0.0180	35	

Table 3 – *continued*

λ_0 (Å)	Ion	Mult.	λ_{obs}	V_{rad} (km s^{-1})	$F(\lambda)/F(\mathrm{H}ref)^d$	$I(\lambda)/I(\mathrm{H}\beta)^e$	Err (%)^f	Notes
9992.46	O II	G[5]$_0$-2[6]	9991.98	−14.43	1.228	0.0688	15	
9993.02	O II	D[3]$_0$-0[4]	*	*	*	*	*	
9993.21	O II	D[3]$_0$-0[4]	*	*	*	*	*	
10013.62	O II	G[4]$_0$-1[5]	10011.96	−49.70	0.706	0.0396	21	
10030.50	He I	6/7	10029.93	−17.04	6.531	0.366	7	
10033.90	He I	7/7	10033.20	−20.91	2.051	0.115	11	
10052.16	H I	P7	10051.51	−19.24	100.0	5.60	5	
10074.81	He I	5/7	10073.73	−32.17	0.407	0.0228	29	
	?		*	*	*	*	*	
10289.52	[S II]	3F	10288.95	−16.59	19.83	1.105	6	
10314.13	He I	4/6	10313.41	−20.81	3.987	0.222	8	
10323.33	[S II]	3F	10322.74	−17.09	25.16	1.402	6	
10339.23	[S II]	3F	10338.16	−31.11	22.72	1.266	6	
10373.34	[S II]	3F	10372.66	−19.71	8.937	0.498	6	
10400.35	[N I]	3F	10400.08	−7.77	4.607	0.256	8	
10410.25	[N I]	3F	10409.58	−19.36	3.334	0.186	8	
10670.61	He I	3P$_0$-3S	10670.13	−13.49	0.611	0.0338	23	
10833.31	He I	1/4	10832.78	−14.58	1581	87.39	5	c
10916.03	He I	6/6	10915.88	−4.25	15.73	0.869	6	
10920.05	He I	7/6	10919.35	−19.22	4.086	0.226	8	
10941.09	H I	P6	10940.45	−17.57	174.9	9.650	5	
10993.84	[Se III]	3P-1D	10991.79	−55.90	0.217	0.0120	:	
10999.70	He I	5/6	10998.88	−22.40	0.963	0.0531	17	
11016.09	He I	1S-1P$_0$	11015.21	−23.88	0.898	0.0495	17	
11048.01	He I	1P$_0$-1D	11047.31	−18.86	1.704	0.0939	12	
11290.41	O I	3P-3D$_0$	11288.91	−39.85	3.004	0.165	9	
11471.30	[P II]	3P-1D	11470.11	−31.10	1.802	0.0987	9	
	?		11696.42		0.349	0.0191	34	
11751.45	C I	3D-3F$_0$	11750.50	−24.24	0.369	0.0201	:	
11756.53	C I	3D-3F$_0$	11756.30	−5.87	0.528	0.0288	:	
11758.00	C I	3D-3F$_0$	*	*	*	*	*	
	?		11864.36		16.68	0.909	6	
	?		11870.45		1.055	0.0575	16	
11886.10	[P II]	3P-1D	11885.48	−15.70	7.498	0.409	6	
11942.40	C II	2F$_0$-2G	11940.71	−44.13	1.241	0.0676	14	
11972.28	He I	3P$_0$-3D	11971.73	−13.67	6.372	0.347	6	
12226.29	[Fe II]	a6D-a4D	12224.29	−49.41	1.291	0.0701	14	b
12530.93	He I	1/3	12530.25	−16.21	9.343	0.505	6	
12570.21	[Fe II]	a6D-a4D	12569.22	−24.29	7.507	0.406	6	
12675.32	[Fe II]	a4D-a2G	12674.46	−20.26	0.304	0.0164	37	
	?		12692.18		7.174	0.387	6	
12706.91	[Fe II]	a6D-a4D	*	*	*	*	*	
12788.42	He I	6/5	12787.88	−12.60	23.28	1.256	5	
12794.00	He I	7/5	12793.26	−17.34	8.353	0.451	6	
12821.59	H I	P5	12821.01	−13.48	344.2	18.57	5	
12849.46	He I	3P$_0$-3S	12847.83	−37.99	1.623	0.0875	12	
12946.20	[Fe II]	a6D-a4D	12944.82	−32.66	1.205	0.0649	15	
12971.98	He I	1P$_0$-1D	12971.62	−8.26	1.559	0.0840	13	
12988.43	He I	5/5	12987.38	−24.28	2.013	0.108	11	
13005.69	[Fe II]	a4D-a2G	13001.23	−102.81	0.306	0.0165	37	
13167.49	O I	3P-3S$_0$	13167.56	1.59	3.870	0.208	8	
13168.46	O I	3P-3S$_0$	*	*	*	*	*	
13168.73	O I	3P-3S$_0$	*	*	*	*	*	
13209.15	[Fe II]	a6D-a4D	13207.77	−31.36	2.044	0.110	11	
13281.40	[Fe II]	a6D-a4D	13280.21	−26.94	0.714	0.0384	21	
13417.97	[Fe II]	a4D-a2G	13415.37	−58.09	0.385	0.0206	32	
14819.71	H I	Br32	14819.41	−6.16	7.192	0.0647	16	
14835.15	H I	Br31	14835.19	0.77	3.229	0.0291	24	
14852.20	H I	Br30	14851.12	−21.71	8.267	0.0744	15	
14871.08	H I	Br29	14870.04	−20.93	8.494	0.0764	15	
14892.08	H I	Br28	14891.49	−11.86	8.408	0.0757	15	
14915.52	H I	Br27	14914.91	−12.17	5.233	0.0471	19	
14941.81	H I	Br26	14941.58	−4.67	8.123	0.0731	15	
14971.42	H I	Br25	14970.50	−18.44	11.057	0.0995	12	

Table 3 – *continued*

λ_0 (Å)	Ion	Mult.	λ_{obs}	V_{rad} (km s^{-1})	$F(\lambda)/F(\mathrm{H}ref)^d$	$I(\lambda)/I(\mathrm{H}\beta)^e$	Err (%)^f	Notes
15004.96	H I	Br24	15004.16	−15.98	10.549	0.0949	12	
15043.15	H I	Br23	15042.23	−18.34	10.486	0.0944	12	
15078.36	He I	3F$_0$-3D	15077.41	−18.88	3.587	0.0323	22	
15086.89	H I	Br22	15086.54	−7.00	17.292	0.156	10	
15087.77	He I	1S-1P$_0$	*	*	*	*	*	
15137.36	H I	Br21	15136.72	−12.59	12.70	0.114	11	
15195.99	H I	Br20	15195.17	−16.21	14.45	0.130	11	
15264.71	H I	Br19	15264.82	2.15	25.63	0.231	9	c
15338.94	[Fe II]	a4F-a4D	15338.65	−5.65	7.758	0.0698	14	
15345.98	H I	Br18	15345.41	−11.19	18.02	0.162	10	
15443.14	H I	Br17	15442.70	−8.52	20.58	0.185	10	
15560.70	H I	Br16	15560.13	−11.00	24.90	0.224	9	
15696.27	He I	3F$_0$-3D	15694.61	−31.71	3.998	0.0360	21	
15704.95	H I	Br15	15704.40	−10.50	28.06	0.254	9	
	?		15808.91		3.152	0.0284	25	
15876.18	He I	3F$_0$-3D	15875.02	−21.84	3.596	0.0324	23	
15884.88	H I	Br14	15884.50	−7.17	32.27	0.290	9	
15999.15	[Fe II]	a4F-a4D	15997.91	−23.16	4.330	0.0390	20	
16113.71	H I	Br13	16112.96	−14.03	39.75	0.358	8	c
16402.94	He I	3F$_0$-3D	16401.61	−24.31	3.369	0.0303	25	
16411.67	H I	Br12	16411.20	−8.67	46.06	0.415	8	
16440.02	[Fe II]	a4F-a4D	16438.47	−28.21	22.49	0.202	10	b
	?		16601.43		5.988	0.0539	18	
16642.25	[Fe II]	a4F-a4D	16641.14	−19.99	3.191	0.0287	26	
16773.41	[Fe II]	a4F-a4D	16776.05	47.26	9.247	0.0832	14	
	?		*	*	*	*	*	
16802.44	He I	3F$_0$-3D	16800.92	−27.10	8.137	0.0732	15	
16811.11	H I	Br11	16810.63	−8.60	69.23	0.623	8	
17007.64	He I	3P$_0$-3D	17006.67	−17.18	49.52	0.446	8	
17356.50	He I	3F$_0$-3G	17355.82	−11.70	10.66	0.0959	14	
17366.85	H I	Br10	17365.92	−16.09	100	0.900	8	
17454.15	[Fe II]	a4F-a4D	17454.94	13.55	5.766	0.0513	19	
17454.43	He I	3S-3P$_0$	*	*	*	*	*	
	?		17639.98		10.59	0.0919	14	
	?		19366.14		0.520	0.0145	33	
19411.45	He I	3D-3F$_0$	19409.76	−26.10	0.883	0.0247	23	
19418.88	He I	1D-1F$_0$	19416.10	−42.92	1.379	0.0386	17	
19438.91	He I	3F$_0$-3G	19438.54	−5.71	3.292	0.0922	10	
19450.87	H I	Br8	19449.19	−25.88	38.53	1.079	5	
19548.63	He I	3D-3P$_0$	19546.85	−27.23	12.31	0.345	6	
20430.41	He I	3S-3P$_0$	20429.07	−19.68	1.148	0.0321	19	
20586.90	He I	1S-1P$_0$	20586.02	−12.88	73.02	2.045	5	
20607.36	He I	3P$_0$-3D	20605.64	−25.00	1.552	0.0435	16	
21125.89	He I	3P$_0$-3S	21124.68	−17.10	5.330	0.149	8	
21137.80	He I	1P$_0$-1S	21136.21	−22.53	1.809	0.0507	14	
21209.90	H$_2$	1-0 S(1)	21213.18	46.36	1.181	0.0331	19	
21613.69	He I	3D-3F$_0$	21612.37	−18.31	3.788	0.106	9	
21622.91	He I	1D-1F$_0$	21621.48	−19.76	1.327	0.0372	17	
21647.45	He I	3F$_0$-3G	21646.63	−11.39	13.45	0.377	6	
21661.20	H I	Br7	21660.35	−11.78	100	2.800	5	
21986.00	[Kr III]	3P-3P	21985.13	−11.86	1.986	0.0556	14	
22186.75	[Fe III]	3H-3G	22185.58	−15.86	0.740	0.0207	26	
22864.00	[Se IV]	–	22860.22	−49.56	2.952	0.0827	11	
23066.55	H I	Pf46	23068.02	19.17	0.303	0.0085	:	
	?		*	*	*	*	*	
23078.95	H I	Pf46	23078.65	−3.83	0.261	0.0073	:	
	?		*	*	*	*	*	
23092.22	H I	Pf44	23092.20	−0.19	0.191	0.0053	:	
23106.44	H I	Pf43	23105.93	−6.59	0.282	0.0079	:	
23121.71	H I	Pf42	23120.41	−16.83	0.311	0.0087	:	
23138.13	H I	Pf41	23136.73	−18.17	0.396	0.0111	39	
23140.77	He I	3D-3F$_0$	*	*	*	*	*	
23151.23	He I	3P$_0$-3D	23153.83	33.72	0.465	0.0130	35	
23155.83	H I	Pf40	*	*	*	*	*	

Table 3 – *continued*

λ_0 (Å)	Ion	Mult.	λ_{obs}	V_{rad} (km s^{-1})	$F(\lambda)/F(\mathrm{H}ref)^d$	$I(\lambda)/I(\mathrm{H}\beta)^e$	Err (%)^f	Notes
23161.39	He I	3D-3F$_0$	*	*	*	*	*	
23174.94	H I	Pf39	23172.04	−37.46	0.873	0.0244	23	
23195.61	H I	Pf38	23192.57	−39.23	0.664	0.0186	28	
23218.02	H I	Pf37	23215.04	−38.42	0.894	0.0250	23	
23242.37	H I	Pf36	23238.49	−50.02	0.809	0.0226	24	
23268.90	H I	Pf35	23264.42	−57.66	0.802	0.0225	24	
23297.87	H I	Pf34	23292.79	−65.32	0.927	0.0259	22	
23329.59	H I	Pf33	23324.07	−70.99	1.031	0.0289	21	
23364.44	H I	Pf32	23358.47	−76.61	1.193	0.0334	19	
23402.83	H I	Pf31	23396.35	−83.06	1.151	0.0322	19	
23445.28	H I	Pf30	23437.89	−94.46	1.377	0.0386	17	
23492.37	H I	Pf29	23483.66	−111.10	1.957	0.0548	14	
23544.81	H I	Pf28	23537.81	−89.14	1.522	0.0426	16	
23603.47	H I	Pf27	23596.44	−89.25	1.621	0.0454	15	
23669.37	H I	Pf26	23662.81	−83.03	1.942	0.0544	14	
23730.67	He I	3F$_0$-3D	23724.99	−71.81	0.259	0.0073	:	
23743.77	H I	Pf25	23737.93	−73.73	1.924	0.0539	14	
23828.23	H I	Pf24	23824.48	−47.19	2.534	0.0709	12	
23924.68	H I	Pf23	23922.53	−26.88	2.507	0.0702	12	
24035.52	H I	Pf22	24037.76	27.90	2.669	0.0747	11	
24065.96	H$_2$	1-0 Q(1)	24069.60	45.34	0.862	0.0241	23	
24163.85	H I	Pf21	24173.09	114.61	2.337	0.0654	12	
24243.61	H$_2$	1-0 Q(3)	24245.20	19.61	1.544	0.0432	16	
24313.62	H I	Pf20	24331.63	222.07	3.688	0.103	10	
	?		24493.32		1.019	0.0285	21	
24490.00	H I	Pf19	24522.68	400.02	4.336	0.121	9	
24699.87	H I	Pf18	24753.25	647.86	5.309	0.149	8	

Notes. ^{a}Affected by charge transfer.
^{b}Affected by telluric emission.
^{c}Affected by atmospheric absorption bands.
^{d}Where F is the unreddened flux measured against the reference line
^{e}Where I is the reddened corrected flux, in units of $100.00 = 1.032 \times 10^{-11}$ erg cm^{-2} s^{-1}.
^{f}Colons indicates errors larger than 40 per cent.

Table 4. Comparison of observed line ratios and those predicted by the CLOUDY model.

Ion	Line ratio	Model	Obs.
He I	6934/7161	0.437	0.448
He I	7161/7816	0.308	0.263
He I	10999/12988	0.426	0.492
[N II]	5755/6538	0.0918	0.0816
[O II]	3726/3729	2.482	2.494
[O III]	4363/5007	0.0048	0.0045
[S II]	6731/6716	2.183	2.014
[S III]	6312/9069	0.0619	0.0571
[Cl III]	5538/5518	2.823	2.900
[Ar III]	5192/7136	0.0057	0.0043
[Ar IV]	4740/4711	3.200	3.398

details on the identification of these lines in the UVES and FIRE spectra.

We identify lines of two ions of Kr. We detect the [Kr III] 2.1986 μm line in the NIR spectrum. This line and the [Se IV] 2.2864 μm line were first identified by Dinerstein (2001), and are the most widely detected n-capture emission lines in PNe (Sterling & Dinerstein 2008). We also detect the faint [Kr III] λ6826.70 line in our optical UVES spectrum. However, although our optical spectrum is of very high resolution, the velocity field of NGC 5315 broadens emission lines, and the flux of this line can be affected by the faint He I 3s ^{3}S–16p ^{3}P^0 λ6827.88 line (Péquignot &

Baluteau 1994). We used the theoretical ratio between He I lines of the same series (specifically, He I λλ6933.89, 7160.61 and 7816.13) using our CLOUDY model (see previous section) to estimate that this He I line contributes 26 per cent of the total measured flux. The Kr^{2+} abundance calculated with the corrected flux is in good agreement with that from the [Kr III] 2.1986 μm line (see Section 5.1). [Kr III] λ9902.30 also falls in the spectral range of UVES and FIRE but is strongly blended with the relatively bright C II λ9903.46 line. We find that the ratio [Kr III] 9902.30/6826.70 = 0.078 for the assumed physical conditions (see Section 4), and hence [Kr III] λ9902.30 accounts for only 1 per cent of the total measured flux of the line. Therefore, we do not consider this [Kr III] line to be detected. We also detect two [Kr IV] lines, λλ5346.02 and 5867.74, which are the brightest n-capture lines detectable in the optical spectra of PNe (e.g. García-Rojas et al. 2015). Given the relatively high brightness of these lines and the consistency between the computed abundances, we consider them well identified.

Thanks to the wide spectral range covered by our spectra, we detect three lines of Se ions. [Se III] λ8855.28 is detected in both UVES and FIRE spectra. It has almost the same wavelength as a weak He I λ8854.20 line, making its detection a delicate matter (García-Rojas et al. 2015). We used the theoretical ratios, computed with our CLOUDY model, of He I lines belonging to the same series as He I λ8854.20, to correct for the contribution of He I. We find a contribution of 56 per cent of [Se III] emission in the FIRE spectra and 53 per cent in the UVES spectra, and the abundances calculated from both spectra are in good agreement (see Section 5.1).
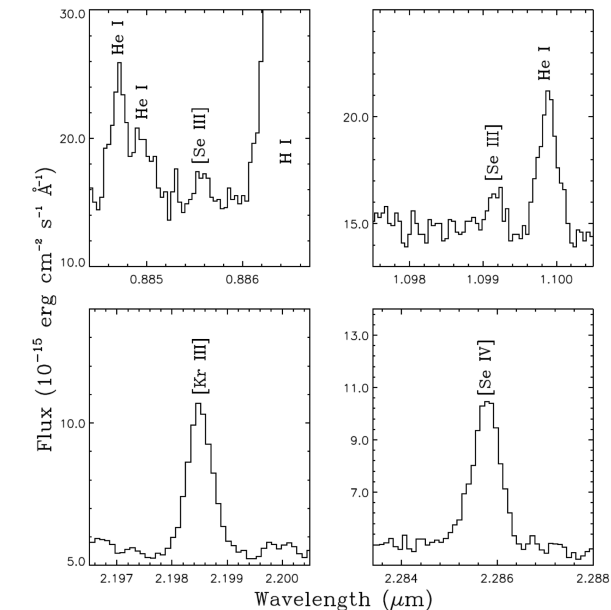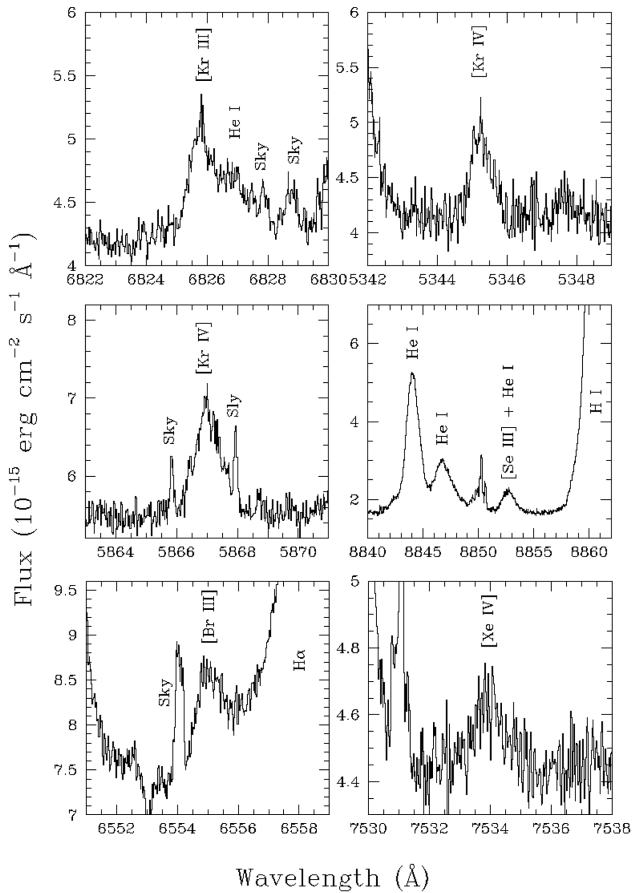
Figure 2. Upper panels: Line profiles of n-capture element ions in the UVES spectrum, including the tentative detection of [Br III] λ6556 line. Lower panels: Detections of Se and Kr ions in the NIR FIRE spectrum.

Table 5. Corrected line ratios [I(Hβ) = 100] for n-capture elements in NGC 5315.

λ₀ (Å)	Ion	$I(\lambda)/I(\mathrm{H}\beta)$	Error (%)[a]
UVES			
5346.02	[Kr IV]	0.0081	20
5867.74	[Kr IV]	0.0188	12
6555.56	[Br III]	0.0097	:
6826.70	[Kr III]	0.0161	16
7535.40	[Xe IV]	0.0032	:
8854.00	[Se III]	0.0055	:
FIRE			
8855.28	[Se III]	0.0062	:
10992.00	[Se III]	0.0120	:
2.1986 μm	[Kr III]	0.0556	13
2.2864 μm	[Se IV]	0.0827	11

Note. [a]Colons indicates errors larger than 40 per cent.

Nevertheless, we note that the line detected at 8855 Å is very faint and therefore the correction made with our photoionization model is very uncertain. Fortunately, we detect another line of Se^{2+} at 10 992 Å in the FIRE spectrum, which is isolated and was recently identified in NGC 5315 by Sterling et al. (2017). We also detect the [Se IV] 2.2864 μm line.

We possibly detect [Xe IV] λ7535.40 line in our UVES optical spectrum. Unfortunately, the [Xe IV] λ5709.21 line, which comes from the same upper level as [Xe IV] λ7535.40, could not be observed since it is strongly blended with the permitted N II λ5710.77 Å line. We computed [Xe IV] λ5709.21/λ7535.40 = 0.82 for the assumed T_e and n_e (see Section 4). This corresponds to just 8 per cent of the flux measured for the feature at 5710 Å that we attribute to N II λ5710.77 Å, and thus we conclude that [Xe IV] λ5709.21 line is not detected in our spectrum. Despite the non-detection of other Xe features in the spectrum of NGC 5315, there are no reasonable alternative identifications to the 7535.40 line, and hence we identify it as [Xe IV]. On the other hand, owing to the ionization degree of NGC 5315, Xe^{2+} should be more abundant than Xe^{3+}. Therefore, we expect to detect the [Xe III] λ5846.77 line, which would strengthen the identification of the [Xe IV] λ7535.40 line. Unfortunately, the [Xe III] λ5846.77 line lies on a continuum bump due to the extremely broad stellar C IV λ5808 line (the red bump of a [WC]-type star) which hampers any detection of faint lines.

We also detect a feature that can be identified as [Br III] λ6555.56. However, we do not detect [Br III] λ6130.40 and therefore we cannot claim this as an unambiguous detection.

We do not detect any emission line from Rb ions. We estimate an upper limit flux of [Rb IV] λ5759.55 line using a 3σ criterion. We assume that the S/N in this region is too low to detect this line. Therefore, this estimation represents the maximum flux expected at that wavelength taking in account the continuum noise in that region. We also tried to estimate an upper limit to the [Rb IV] λ1.5973 μm line, but the telluric correction around this line was unreliable and an estimation of an upper limit is not possible.

4 PHYSICAL CONDITIONS

Physical conditions were computed using flux ratios of ions which are sensitive to electron temperature and/or to electron density. The computations were carried out with PYNEB v1.0.26 (Luridiana, Morisset & Shaw 2015), using the atomic data presented in Table 6. The electron density n_e and temperature T_e were estimated following

Table 6. Atomic data set used for collisionally excited lines.

Ion	Transition probabilities	Collisional strengths
N^+	Froese Fischer & Tachiev (2004)	Tayal (2011)
O^+	Froese Fischer & Tachiev (2004)	Kisielius et al. (2009)
O^{2+}	Froese Fischer & Tachiev (2004)	Storey, Sochi & Badnell (2014)
	Storey & Zeippen (2000)	
Ne^{2+}	Galavís, Mendoza & Zeippen (1997)	McLaughlin & Bell (2000)
S^+	Podobedova, Kelleher & Wiese (2009)	Tayal & Zatsarinny (2010)
S^{2+}	Podobedova et al. (2009)	Tayal & Gupta (1999)
Cl^+	Mendoza & Zeippen (1983)	Tayal (2004)
Cl^{2+}	Mendoza (1983)	Butler & Zeippen (1989)
Cl^{3+}	Kaufman & Sugar (1986)	Galavís, Mendoza & Zeippen (1995)
	Mendoza & Zeippen (1982a)	
	Ellis & Martinson (1984)	
Ar^{2+}	Mendoza (1983)	Galavís et al. (1995)
	Kaufman & Sugar (1986)	
Ar^{3+}	Mendoza & Zeippen (1982b)	Ramsbottom & Bell (1997)
Fe^{2+}	Quinet (1996)	Zhang (1996)
	Johansson et al. (2000)	
Se^{2+}	Sterling et al. (2017)	Sterling et al. (2017)
Se^{3+}	Biémont & Hansen (1986b)	Schoning (1997)
Kr^{2+}	Biémont & Hansen (1986b)	Schoning (1997)
Kr^{3+}	Biémont & Hansen (1986a)	Schoning (1997)
Br^{2+}	Biémont & Hansen (1986a)	Schoning (1997)[a]
Xe^{3+}	Biémont et al. (1995)	Schoening & Butler (1998)

Note. [a]Scaled from Kr^{3+} effective collision strengths.

Table 7. Physical conditions in NGC 5315.

Diagnostic	
n_e (cm^{-3})	
[O II] λ3726/λ3729	30225^{+25500}_{-7900}
[S II] λ6731/λ6716	9400:
[Fe II][a]	30000 ± 7000
[Cl III] λ5538/λ5518	26800^{+9000}_{-6500}
n_e(low-mid) (adopted)	**26800^{+9000}_{-6500}**
[Ar IV] λ4740/λ4711	38150^{+12500}_{-9850}
n_e(high) (adopted)	**38150^{+12500}_{-9850}**
T_e (K)	
[N II] λ5755/λ6584	9850 ± 625
T_e(low) (adopted)	**9850 ± 625**
[O III] λ4363/λλ5007	8700 ± 200
[Ar III] λ5192/λ7136	8350 ± 350
[S III] λ6312/λ9069	8975 ± 350
T_e(mid-high) (adopted)	**8650 ± 200**

Note. [a]Average value between different diagnostics (see the text). Colons indicate very uncertain determinations.

the methodology described in previous works of our group (e.g. García-Rojas et al. 2015). As in Peimbert et al. (2004), we initially assumed three different zones in NGC 5315, characterized by low (ionization potential IP < 17 eV), medium (17 eV < IP < 39 eV) and high (IP > 39 eV) ionization. However, given the relatively low excitation of NGC 5315, and the similarities between different diagnostics, we adopted a two-zone model for n_e (low-medium and high ionization zones) and T_e (low and medium-high ionization zones) (see Table 7).

It is well known that the auroral [N II] λ5755 line is affected by recombination. We use equation (1) of Liu et al. (2000) to compute the recombination contribution so that this line can be used for

the T_e computation. Since permitted N II lines can be affected by fluorescence effects in relatively low ionization PNe (see Escalante, Morisset & Georgiev 2012), we made a preliminary computation of the N^{2+}/H^+ ratio by assuming N^{2+}/O^{2+} (recombination lines) $\approx$ N^+/O^+ (collisionally excited lines, CELs). We find a recombination contribution of less than 5 per cent of the λ5755 flux, and therefore neglect it. We computed T_e with the diagnostic [S III] 6312/9069 using [S III] λ6312 from UVES and [S III] λ9069 from FIRE data. Unfortunately, the [S III] λ9069 line in the UVES spectrum is contaminated by atmospheric absorption and cannot be used. Moreover, the [S III] λ9530 line in the UVES spectrum is saturated and its measured flux is unreliable. As can be seen in Table 7, T_e([S III]) is in good agreement with T_e([O III]) and T_e([Ar III]), calculated using lines from UVES data. A diagnostic diagram for NGC 5315 is shown in Fig. 3.

Given the high density of NGC 5315, the low ionization [O II] λ3726/λ3729 and [S II] λ6731/λ6716 n_e diagnostics are saturated, as it is clearly visible from the huge uncertainties of these ratios in Table 7. Therefore, we decided to use the density found with the [Cl III] λ5538/λ5518 diagnostic as representative of the low-medium ionization zone.

We also calculated n_e using [Fe II] line ratios from our FIRE data, which are useful diagnostics for a large range of densities. Using PYNEB and the atomic data set of Fe^+ by Bautista et al. (2015), we derive an electron density of $30\,000 \pm 7000$ cm^{-3}, which is the average of the values from the [Fe II] 1.2946 μm/1.2570 μm, 1.3281 μm/1.2570 μm, 1.5339 μm/1.2570 μm and 1.5999 μm/1.2570 μm diagnostics. This determination is consistent with the optical density diagnostics of the low-medium ionization zone (see Table 7).

The uncertainties in the physical conditions were calculated using Monte Carlo simulations. For each line flux involved in these calculations, we generated 10 000 random values with a Gaussian distribution centred on the observed value with a sigma corresponding to
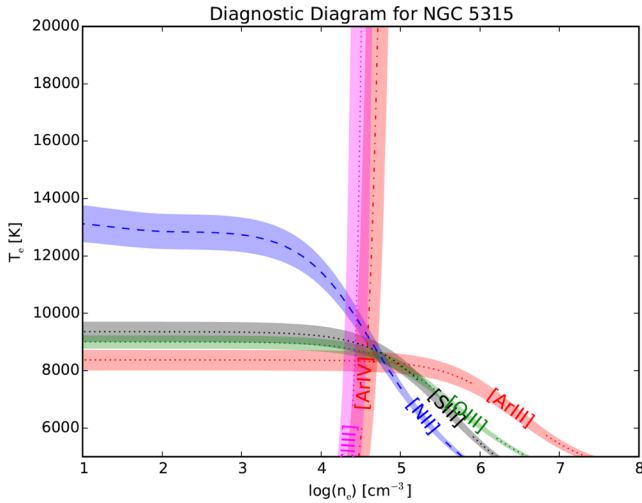
Figure 3. Diagnostic diagram for the complete set of ionization zones for NGC 5315. Different colours are used for different elements, and different line styles correspond to different ions.

the line flux error. The physical conditions with their uncertainties are presented in Table 7.

5 IONIC ABUNDANCES

5.1 Collisionally excited lines

Ionic abundances were calculated using CELs, for N, O, Ne, S, Cl, Ar, P, Fe, Se, Br, Kr and Xe ions. Based on the IP of the ions, we choose physical conditions of low ionization (IP < 17 eV) for N^+, O^+, P^+, S^+, Cl^+, Fe^+ and Fe^{2+}; medium ionization (17 eV < IP < 39 eV) for O^{2+}, S^{2+}, Cl^{2+}, Cl^{3+}, Ar^{2+}, Se^{2+}, Se^{3+}, Br^{2+} and Kr^{3+}; and high ionization (IP > 39 eV) for Ne^{2+} and Ar^{3+}. Computations were carried out using PYNEB and the atomic data used are presented in Table 6. Uncertainties in the line intensities and physical conditions were propagated via Monte Carlo simulations. Ionic abundances from CELs are presented in Table 8.

To investigate the extent to which the different slit positions used for the UVES and FIRE observations affect our results, we compare the abundances of ions detected in both data sets (Cl^+, Cl^{2+}, P^+, Fe^+, Se^{2+} and Kr^{2+}). As can be seen in Table 9, our optical ionic fractions from UVES spectrum are similar to both the FIRE and the Peimbert et al. (2004) data [our NIR observations were performed using a slit position similar to Peimbert et al. (2004)]. In order to be consistent with our results, for this comparison we re-computed the ionic abundances from Peimbert et al. (2004) spectra, using our atomic data set. In Table 8, we can check that the abundances obtained from optical and NIR lines of Cl^+, Cl^{2+}, P^+ and Fe^{2+} are in generally good agreement within uncertainties.

For *n*-capture element ions, we emphasize the good agreement between the abundances of Kr^{2+} obtained from lines measured in the optical and in the NIR ranges, as well as the abundances obtained using the two available Kr^{3+} lines in the optical. We also find good agreement between the Se^{2+}/H^+ abundances derived from [Se III] $\lambda 8855$ in the UVES and FIRE spectra [$12+\log(Se^{2+}/H^+) = 3.11$ and 3.16, respectively]. The Se^{2+} abundance derived from this line is ~ 0.2 dex lower than that computed from the [Se III] $\lambda 1.0992\,\mu$m line, which we attribute to the uncertain correction for the contribution of He I to the $\lambda 8854.20$ flux. We therefore choose

Table 8. Ionic abundances from CELs in units of $12 + \log(X^{i+}/H^+)$.

Ion	Line used	Abu.UVES	Abu.FIRE
N^+	$\lambda 6548$	7.67 ± 0.08	
N^+	$\lambda 6584$	7.70 ± 0.08	
N^+	**(adopted)**	**7.69 ± 0.08**	
O^+	$\lambda 3726$	$7.96^{+0.17}_{-0.15}$	
O^+	$\lambda 3729$	$7.96^{+0.17}_{-0.15}$	
O^+	**(adopted)**	**7.96 ± 0.17**	
O^{2+}	$\lambda 4959$	8.70 ± 0.05	
O^{2+}	$\lambda 5007$	8.72 ± 0.05	
O^{2+}	**(adopted)**	**8.71 ± 0.05**	
Ne^{2+}	$\lambda 3868$	8.11 ± 0.07	
Ne^{2+}	$\lambda 3968$	8.11 ± 0.07	
Ne^{2+}	**(adopted)**	**8.11 ± 0.07**	
P^+	$\lambda 7876$	4.10 ± 0.12	
P^+	$\lambda 11470$		4.09 ± 0.06
P^+	$\lambda 11886$		4.28 ± 0.06
P^+	**(adopted)**	**4.24 ± 0.09**	
S^+	$\lambda 6716$	$6.39^{+0.12}_{-0.10}$	
S^+	$\lambda 6731$	$6.35^{+0.12}_{-0.10}$	
S^+	**(adopted)**	**6.36 ± 0.12**	
S^{2+}	$\lambda 9069$		7.08 ± 0.03
S^{2+}	$\lambda 9530$		7.13 ± 0.03
S^{2+}	**(adopted)**	**7.11 ± 0.03**	
Cl^+	$\lambda 9123$	4.33 ± 0.07 **4.35 ± 0.07**	4.37 ± 0.07
Cl^{2+}	$\lambda 3353$	$5.16^{+0.13}_{-0.11}$	
Cl^{2+}	$\lambda 5517$	5.29 ± 0.08	
Cl^{2+}	$\lambda 5538$	5.29 ± 0.05	
Cl^{2+}	$\lambda 8434$	$5.20^{+0.11}_{-0.09}$	
Cl^{2+}	$\lambda 8484$	$5.31^{+0.11}_{-0.09}$	$5.42^{+0.12}_{-0.10}$
Cl^{2+}	**(adopted)**	**5.29 ± 0.07**	
Cl^{3+}	**$\lambda 8046$**	**3.86 ± 0.06**	
Ar^{2+}	$\lambda 7135$	6.61 ± 0.05	
Ar^{2+}	$\lambda 7751$	6.62 ± 0.05	
Ar^{2+}	**(adopted)**	**6.61 ± 0.05**	
Ar^{3+}	$\lambda 4711$	4.92 ± 0.10	
Ar^{3+}	$\lambda 4740$	4.92 ± 0.06	
Ar^{3+}	**(adopted)**	**4.92 ± 0.08**	
Fe^+	$\lambda 7154$	$5.05^{+0.12}_{-0.08}$	
Fe^+	$\lambda 8619$		5.12 ± 0.07
Fe^+	$1.2570\,\mu$m		5.17 ± 0.06
Fe^+	$1.2946\,\mu$m		5.18 ± 0.07
Fe^+	$1.3209\,\mu$m		5.16 ± 0.07
Fe^+	$1.3281\,\mu$m		5.20 ± 0.09
Fe^+	$1.5339\,\mu$m		5.21 ± 0.07
Fe^+	$1.5999\,\mu$m		5.15 ± 0.09
Fe^+	$1.6642\,\mu$m		5.35 ± 0.11
Fe^+	**(adopted)**	**5.15 ± 0.08**	
Fe^{2+}	$\lambda 4701$	5.01 ± 0.10	
Fe^{2+}	$\lambda 4881$	5.09 ± 0.10	
Fe^{2+}	$\lambda 5270$	4.96 ± 0.11	
Fe^{2+}	$2.2187\,\mu$m		5.24 ± 0.15
Fe^{2+}	**(adopted)**	**5.05 ± 0.12**	
Se^{2+}	$\lambda 8855$	3.11:	3.16:
Se^{2+}	$1.0995\,\mu$m		3.33 ± 0.16
Se^{2+}	**(adopted)**	**3.33 ± 0.16**	
Se^{3+}	**$2.2864\,\mu$m**		**2.90 ± 0.05**
Br^{2+}	$\lambda 6556$	2.97:	
Kr^{2+}	$\lambda 6826$	3.34 ± 0.07	
Kr^{2+}	$2.1986\,\mu$m		3.39 ± 0.06
Kr^{2+}	**(adopted)**	**3.38 ± 0.06**	
Kr^{3+}	$\lambda 5346$	3.00 ± 0.09	
Kr^{3+}	$\lambda 5867$	3.12 ± 0.06	
Kr^{3+}	**(adopted)**	**3.08 ± 0.08**	
Rb^{3+}	**$\lambda 5759$**	**<2.80**	
Xe^{3+}	**$\lambda 7535$**	**2.38:**	

Note. Colons indicate very uncertain abundances.

Table 9. Comparison of ionic abundance ratios. The lines used to compute ionic abundances are listed in Table 8.

Ratio	UVES	FIRE	Peimbert et al. (2004)[a]
O^+/O^{2+}	0.204 ± 0.088	–	0.153
Cl^{3+}/Cl^{2+}	0.037 ± 0.009	–	0.036
Cl^+/Cl^{2+}	0.110 ± 0.028	0.089 ± 0.032	0.089
Ar^{3+}/Ar^{2+}	0.020 ± 0.005	–	0.011
Fe^+/Fe^{2+}	1.041 ± 0.442	0.844 ± 0.388	–

Note. [a]Computed with atomic data shown in Table 6.

Table 10. Atomic data set used for recombination lines.

Ion	Recombination coefficients
H^+	Storey & Hummer (1995)
He^+	Porter et al. (2012, 2013)
C^{2+}	Davey, Storey & Kisielius (2000)
N^{2+}	Fang et al. (2011), Fang, Storey & Liu (2013)
O^{2+}	Storey (1994)
	Liu et al. (1995)
Ne^{2+}	Kisielius et al. (1998)
	Kisielius & Storey (private communication)
Mg^{2+}	Kisielius et al. (1998)

to use the Se^{2+} abundance obtained from the [Se III] $\lambda 1.0992$ μm line in our analysis.

We also report the abundances of other three A-capture element ions. We calculate the abundance of Br^{2+} using the [Br III] $\lambda 6556$ line and collision strengths scaled from Kr^{3+} (see Table 6). The abundance of Xe^{3+} is calculated using the flux measured for the very faint [Xe IV] $\lambda 7535.40$ line. Finally, Rb^{3+} is calculated from an upper limit flux estimation of the [Rb IV] $\lambda 5759.55$ line.

The FIRE NIR spectrum exhibits multiple [Fe II] lines, which can be used as density diagnostics since they are not prone to fluorescent effects that contaminate optical [Fe II] lines. The ratio of two lines arising from the same upper level is given by ratio of transition probabilities. So, the expected [Fe II] 1.2570 μm/1.6442 μm, 1.3209 μm/1.6442 μm, 1.3209 μm/1.2570 μm, 1.2946 μm/1.3281 μm and 1.2946 μm/1.5339 μm line ratios are 1.30, 0.35, 0.26, 1.77 and 1.00, respectively, using the transition probabilities of Bautista et al. (2015). The observed line ratios appear to be con-

sistent, within the uncertainties, with the theoretical ones. In particular, the [Fe II] 1.3209 μm/1.2570 μm, 1.2946 μm/1.3281 μm and 1.2946 μm/1.5339 μm line ratios are 0.27 ± 0.04, 1.70 ± 0.40 and 0.83 ± 0.16, respectively, which are in good agreement with theoretical expectations, whereas the [Fe II] 1.2570 μm/1.6442 μm and 1.3209 μm/1.6442 μm line ratios present values of 1.79 ± 0.20 and 0.48 ± 0.07, both higher than the theoretical ones. This is probably owing to an inaccurate subtraction of telluric emission nearby the [Fe II] 1.6442 μm line that makes the flux measured for this line unreliable. In Table 8, we present the results obtained from individual [Fe II] lines in both the UVES and FIRE wavelength ranges.

5.2 Optical recombination lines

We calculate ionic abundances using He, C, N, O and Ne optical recombination lines (ORLs). The atomic data used are shown in Table 10. We detect several permitted lines of heavy-element ions, such as C II, N II, N III, O I, O II, O III, Ne II and Mg II, but some are affected by fluorescence or contaminated by telluric features. We only consider pure recombination lines in these calculations. Discussion about the formation mechanism of several permitted lines can be found in Esteban et al. (1998, 2004). In Fig. 4, we show the brightest C II and O II lines in our optical spectrum. The high resolution of the data allows to deblend the multiple features in the region of the multiprlet 1 O II lines.

The abundance discrepancy problem arises from the fact that ORLs provide ionic abundances that are systematically larger than those obtained from CELs in photoionized nebulae, whether H II regions or PNe. Solving this problem has critical implications for the measurement of the chemical content of nearby and distant galaxies, which is most often done using CELs from their ionized interstellar medium. Three main scenarios have been proposed to explain this discrepancy: (a) the existence of temperature fluctuations over the observed volume of the nebula (Peimbert 1967; Torres-Peimbert, Peimbert & Daltabuit 1980); (b) cold and dense H-poor inclusions in which the bulk of the ORL emission originates (e.g. Liu et al. 2000) and, (c) the departure of the free electron energy distribution from the Maxwellian distribution (κ-distribution, see Nicholls, Dopita & Sutherland 2012). While there is no direct observational evidence that favours or discards any of these scenarios, indirect evidence
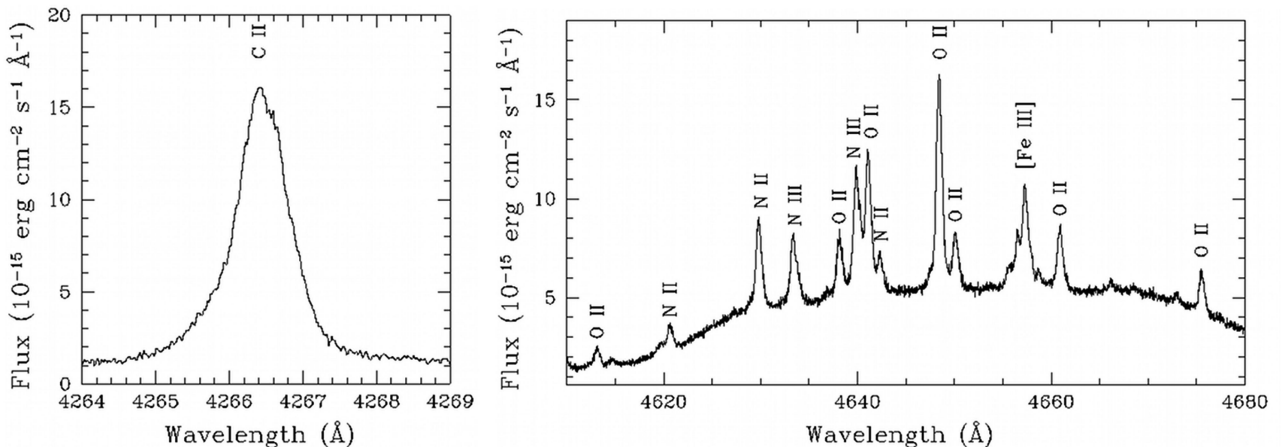
Figure 4. Portion of the echelle optical spectra of NGC 5315, showing the zone where the C II $\lambda 4267$ line and the multiplet 1 O II lines lie. A bump in the continuum in the right plot is apparent, and arises from a strong stellar feature, which is a blend of stellar C III, C IV and He II broad emission lines (Marcolino et al. 2007).

suggests that metal-rich inclusions may be the source of abundance discrepancy factors (ADFs) in PNe (Tsamis et al. 2004; Wang & Liu 2007; García-Rojas et al. 2016).

Importantly, previous studies have shown that the ADFs of C, N and O ions in Galactic PNe are very similar (Liu et al. 2000; Wang & Liu 2007), and hence abundance ratios found from ORLs are suitable proxies for CEL abundance ratios. This is most relevant in the case of C/O, since no CELs of C ions lie in the UVES/FIRE spectral range.

NGC 5315 has a relatively low degree of ionization, and thus we do not detect He II lines. He$^+$ abundances are computed with PYNEB, using the three brightest He I lines $\lambda\lambda$4471, 5876 and 6678. The effects of collisional contributions and optical depth in the triplet lines are considered. Results from the three lines are very consistent and are shown in Table 11.

C^{2+} abundances from ORLs are in very good agreement between lines belonging to different multiplets (see Table 11). C II λ9903.46 is blended with the very faint [Kr III] λ9902.30 line. Although this contribution should be negligible, we do not consider this line, because it yields a higher abundance from FIRE data than from UVES data. We ascribe this discrepancy to atmospheric absorption effects visible in the 2D optical spectrum. In general, C^{2+} abundances from ORLs are in very good agreement with those computed by Peimbert et al. (2004) for this object.

Fang, Storey & Liu (2011) compute very detailed recombination coefficients for N II lines. We have used these atomic data to compute N^{2+} abundances from multiplet 3 N II lines. We find an excellent agreement between all the lines of the multiplet.

To compute O^{2+} abundances from ORLs, we use lines from multiplets 1, 2, 10 and 20 as recommended by Esteban et al. (2004). Given the high density of NGC 5315, departures from LTE for O II multiplet 1 (Ruiz et al. 2003; Tsamis et al. 2004) that are important when $n_e < 10^4$ cm^{-3} can be ignored. The agreement in O^{2+} abundances derived from the different multiplet 1 lines shows that this is a good assumption (Table 11). We use recombination coefficients assuming LS-coupling from Storey (1994) for 3s–3p transitions (multiplets 1 and 2), and the intermediate-coupling scheme by Liu et al. (1995) for 3p–3d transitions (multiplets 10 and 20). Results are shown in Table 11.

We compute Ne^{2+} abundances from ORLs using lines of multiplets 1, 39, 55 and 57. A detailed discussion of the excitation mechanisms of these lines can be found in García-Rojas et al. (2015). We use recombination coefficients by Kisielius et al. (1998) for multiplets 1 and 39 and those by Kisielius (private communication) for multiplets 55 and 57. We adopted the average abundance given from all these multiplets.

Finally, we estimate Mg^{2+} abundance from the Mg II 3d–4f λ4481 line. For this ion there are no recombination coefficients available, so we assume that the Mg II λ4481 line has an effective recombination coefficient equal to that of the C II λ4267 line (Barlow et al. 2003; Wang & Liu 2007).

6 TOTAL ABUNDANCES

To compute total abundances, we have to take unobserved ions into account. In general for the most common elements, we used the detailed ICFs provided by Delgado-Inglada, Morisset & Stasińska (2014, hereinafter D-I14) to correct for the presence of unobserved ions. However, we make an exception for N (see below). In Table 12, we present the total abundances we computed for NGC 5315. The first four columns of Table 12 present the abundances obtained from our data from both CELs and ORLs, either by

Table 11. Ionic abundances from ORLs.

Mult.	λ_0 (Å)	X^{i+}/H$^+$ (10^{-5})
	He$^+$	
14	4471	12267 ± 860
11	5876	13150 ± 924
46	6678	12219 ± 853
	Adopted	**12819 ± 880**
	C^{2+}	
6	4267.15	**66 ± 5**
16.04	6151.43	**61 ± 6**
17.02^a	9903.46	77 ± 6
17.06	5342.38	**62 ± 6**
	Adopted	**63 ± 6**
	N^{2+}	
3	5666.64	61 ± 6
	5676.02	48 ± 7
	5679.56	49 ± 5
	5686.21	53 ± 8
	5710.76	51 ± 8
	5730.65	69:
	Adopted	**52 ± 4**
	O^{2+}	
1	4638.85	89 ± 11
	4641.81	80 ± 7
	4649.14	81 ± 6
	4650.84	87 ± 11
	4661.64	83 ± 9
	4676.24	61 ± 9
	Sum	**81 ± 7**
2^b	4317.14^d	84 ± 18
	4319.63	59 ± 14
	4325.76^c	242 ± 73
	4336.83	76 ± 28
	4345.56	103 ± 19
	4349.43	65 ± 9
	4366.89	116 ± 19
	Sum^e	**81 ± 17**
10^b	4072.15	**81 ± 9**
	4092.93	66:
20	4110.79	121 ± 8
	4019.22	59 ± 12
	Average	**81 ± 12**
	Adopted	**81 ± 12**
	Ne^{2+}	
1	3694.22	21 ± 6
	3709.62	27 ± 9
	3766.26	25 ± 10
	3777.14	27 ± 11
	sum	**24 ± 6**
39	3829.77	18:
55	4409.30	**11 ± 4**
57	4428.77	4:
	adopted	**19 ± 6**
	Mg^{2+}	
1	4481.21	3.6 ± 0.8

Notes. ^{a}Blended with [Kr III] λ9902.30.
^{b}Assuming case A.
^{c}Blended (see table 2).
^{d}Affected by charge transfer.
^{e}Without considering blended lines.
Colons indicate very uncertain abundances.

Table 12. Total abundances [12 + log(X/H)].

Element	CELs sum	CELs ICF	ORLs sum	ORLs ICF	PE04[a] CELs	PE04[a] ORLs	PO02[b] CELs	PO02[b] ORLs	T03, T04[c] CELs	T03, T04[c] ORLs	Model
He	–	–	11.11 ± 0.03	–	–	11.09	–	11.09	–	11.08	11.03
C	–	–	8.83 ± 0.05^h	8.89 ± 0.10	–	8.85	8.64	–	8.33	8.86	8.42
N	–	$8.52^{+0.30d}_{-0.21}$	–	$8.79^{+0.16i}_{-0.08}$	–	8.82	8.66	–	8.52	8.77	8.39
O	8.78 ± 0.05	–	8.98 ± 0.06	–	8.63	8.87	8.72	–	8.79	9.10	8.80
Ne	–	8.40 ± 0.12	–	–	8.05	–	8.20	–	8.30	–	8.09
Mg	–	–	7.56 ± 0.10	–	–	–	–	–	–	–	–
P	–	5.06:	–	–	–	–	–	–	–	–	5.30
S	7.18 ± 0.03	–	–	–	7.34	–	7.08	–	7.31	–	7.27
Cl	5.35 ± 0.07	–	–	–	5.36	–	–	–	5.41	–	5.37
Ar	–	6.73 ± 0.22	–	–	6.56	–	6.66	–	6.56	–	6.49
Fe	5.40 ± 0.10	$5.77 \pm 0.22/5.48 \pm 0.17^g$	–	–	–	–	–	–	–	–	5.70
Se	–	3.60 ± 0.17^e	–	–	–	–	–	–	–	–	–
Kr	–	3.60 ± 0.07^f	–	–	–	–	–	–	–	–	–
Xe	–	3.43:	–	–	–	–	–	–	–	–	–
Br	–	3.53:	–	–	–	–	–	–	–	–	–
Rb	–	<2.87	–	–	–	–	–	–	–	–	–

Notes. [a]Peimbert et al. (2004).
[b]Pottasch et al. (2002).
[c]Tsamis et al. (2003, 2004).
[d]Using the ICF N/O = N^+/O^+.
[e]Using the ICFs given by equation (9) of Sterling et al. (2015).
[f]Using the ICF given by equation (4) of Sterling et al. (2015).
[g]Using the ICFs of equation (2)/equation (3) provided by Rodríguez & Rubin (2005).
[h]Scaling C^{2+}/C^+ from CELs using an average value between Dufour et al. (2015) and Pottasch et al. (2002) data.
[i]Assuming N/O = N^{2+}/O^{2+} (ORLs).
Colons indicate very uncertain abundances.

summing the ionic abundances or by applying an ICF. The next columns show the results obtained by Peimbert et al. (2004), Pottasch et al. (2002), Tsamis et al. (2003) and Tsamis et al. (2004). The last column of Table 12 shows the abundances from our optimized CLOUDY model. As can be seen in Table 12, there is general good agreement within the uncertainties between our computed elemental abundances and those derived by our model and in previous works. Below we briefly discuss the most common elements, and in Section 6.1 we discuss elemental abundances of *n*-capture elements.

In the spectrum of NGC 5315, there are no He II lines and ions with similar or higher IP are not seen. Given that $(O^{2+}/(O^++O^{2+})) = 0.85$, the contribution of neutral He to the total He abundance should be negligible (D-I14) and thus we assume that He/H = He^+/H^+.

Similarly, we can disregard the presence of O^{3+} in the nebula. Thus, we computed O abundance from CELs by simply adding O^+ and O^{2+} abundances, which are the only two ions of this element detected in the spectrum of NGC 5315. We estimated O^+ from ORLs by scaling the ratio O^+/O^{2+} computed from CELs. The total O abundance from ORLs is higher, resulting in an abundance discrepancy factor, ADF(O) = 1.58 (see Table 12).

Although C CELs are only detectable in UV spectra, C abundances can also be computed from optical C II and C III ORLs. However, the excitation of NGC 5315 is too low to detect C III RLs. We compute the elemental C abundance using our C^{2+} abundance from C II ORLs and the ICF presented in equation (39) of D-I14. We compare our results with that obtained assuming a simple sum of C^+ and C^{2+} abundances from ORLs; to estimate C^+/H^+, we rescale using the C^+/C^{2+} ratios obtained from CELs by Pottasch et al. (2002) and by Dufour et al. (2015). Both results are in very good agreement with what we found using the ICF correction (see Table 12). Despite the well-known abundance discrepancy problem between

CEL and ORL abundances (see Section 5.2), numerous studies have shown that C/O (and N/O) ratios computed from ORLs are consistent with the ratios derived from CELs (e.g. Tsamis et al. 2004; Wesson, Liu & Barlow 2005; Wang & Liu 2007; Delgado-Inglada & Rodríguez 2014).

To compute the N elemental abundance from optical and NIR spectra is a delicate matter. We have computed N/O using all the available lines and different methods to better constrain this abundance ratio. First, we used the [N II] lines to compute N^+/H^+. D-I14 argue that the classical scheme N/O = N^+/O^+ may underestimate N abundances, especially when the temperature of the central star is low, which is the case when He II lines are not observed, and they proposed a new ICF. However, in a later work, Delgado-Inglada et al. (2015) found that their ICF could introduce an unexpected trend with the degree of ionization in the N/O values obtained for a group of H II regions and PNe. The trend seems to be related to the fact that the nebulae are either matter- or radiation-bounded. The classical ICF seems to produce more accurate results for radiation-bounded nebulae, while the ICF from D-I14 is preferred for matter-bounded nebulae. To better constrain the N ICF, we compared observed ionic fractions (O^{2+}/O^+, S^{2+}/S^+, Ar^{+3}/Ar^{2+} and He^{2+}/He^+) to the grid of photoionization models of D-I14. From our inspection, we concluded that NGC 5315 is most likely radiation-bounded, and hence the classical ICF provides a more reliable value of the N/O in this PN. The derived N/O value from CELs and the classical ICF is 0.55. The uncertainties in log(N/O) associated with this ICF, estimated from the grid of photoionization models by D-I14, are $^{+0.3}_{-0.2}$ dex.

Secondly, our optimized CLOUDY model (Section 3) produces a somewhat lower N abundance than the one derived with the ICF method [12+log(N/H) = 8.39 compared to 8.52], and so is the N/O ratio (0.39). As a third estimate, we computed the total N/O ratio from ORLs (see Table 12). Since permitted optical N I lines

are strongly affected by fluorescence effects, it is not possible to determine the N^+/H^+ abundance from ORLs. Therefore we use the approximation $N/O = N^{2+}/O^{2+}$ for ORLs, which gives a ratio of 0.64. The uncertainties in $\log(N/O)$ associated with this ICF are $^{+0.15}_{-0.05}$ and they were obtained from the D-I14 grid of photoionization models. We use the average N/O ratio weighted by the uncertainties from these estimates, $0.59^{0.24}_{0.15}$, in the remainder of our analysis.

We calculate total abundances of Ne, S, Cl and Ar, using the ICFs developed by D-I14 when needed, or by summing the ionic abundances when a sufficient number of ions are detected. The optical range hosts several [Ne III], [Ne IV] and [Ne V] CELs, but owing to the relatively low ionization degree of NGC 5315 we only detect [Ne III] lines. There are no lines of the Ne^+ ionization stage in our spectral range, and to correct for its contribution we used the ICF given by equation (17) of D-I14. We detect [S II] and [S III] lines in our spectra. D-I14 found that if [S II] and [S III] are seen in the spectra and the object does not show He II emission, more highly charged states have a negligible contribution. Thus, we compute the total S abundance by adding the S^+ and S^{2+} ionic abundances. Our results are consistent with values from literature (see Table 12). Cl ions have several emission lines in the optical range, including [Cl II], [Cl III] and [Cl IV]. The amount of Cl^{4+} is negligible for NGC 5315, because the IP is too high (53.5 eV). We follow the recommendation by D-I14, who suggest that total Cl abundance can be computed as the sum of ionic abundances when [Cl II], [Cl III] and [Cl IV] lines are detected and He II lines are not seen in the spectra. Finally, we detect [Ar III] and [Ar IV] lines. Given the ionization degree of NGC 5315, we have to take into account the contribution of Ar^+, which can be an important contributor to the total abundance of Ar in low ionization PNe. The contribution of Ar^{4+} is negligible owing to its high IP (59.81 eV) and the non-detection of He II lines. We used the ICF shown in equation (36) by D-I14, which is valid when $O^{2+}/(O^++O^{2+}) > 0.5$. The uncertainties associated with this ICF are higher than for other elements (D-I14), but this ionization correction scheme is the best one available for this specie and our result is consistent with values from literature (see Table 12).

We assumed $Mg/H = Mg^{2+}/H^+$ given the wide ionization potential interval occupied by Mg^{2+} (Barlow et al. 2003; Wang & Liu 2007). We obtain $12+\log(Mg/H) = 7.56 \pm 0.10$ (see Table 12). This value is compatible with the solar photospheric value of Asplund et al. (2009) [$12+\log(Mg/H) = 7.60$] and is identical to the average value of the Mg/H ratio in Galactic disc PNe (Wang & Liu 2007).

We used two different ICFs to calculate the total abundance of Fe, equations (2) and (3) of Rodríguez & Rubin (2005). These two ICFs provide a range of Fe abundances. Additionally, we estimate the total Fe abundance from the sum of Fe^+ and Fe^{2+} as 5.40 ± 0.10. This value represents a lower limit of the total abundance of this element, since we ignore the contribution of [Fe IV], whose optical lines are intrinsically weak and were not detected. Furthermore, the contribution of Fe^+ is uncertain, since its lines can arise both from the ionized portion of the nebula and from the neutral and partially molecular region. However, this sum agrees within the uncertainties with the lower limit of Fe abundance obtained from equation (3) of Rodríguez & Rubin (2005).

D-I14 do not provide corrections for unseen ions of P. In order to compute the total abundance of P, we took advantage of the similarity between the IP of P^+ and S^+ using the ionization correction scheme $P/P^+ = S/S^+$. A detailed set of photoionization models is needed to find a more accurate ICF for this element.

Table 13. Kr and Se total abundances [$12 + \log(X/H)$].

ICF[a]	Kr	Se
Equation (1)	3.61 ± 0.07	–
Equation (2)	3.84 ± 0.24	–
Equation (3)	4.17 ± 0.09	–
Equation (4)	3.60 ± 0.07	–
Equation (7)	–	3.89 ± 0.28
Equation (8)	–	3.13 ± 0.11
Equation (9)	–	3.60 ± 0.17

Note. [a]ICFs provided by Sterling et al. (2015).

6.1 Neutron-capture element abundances

The first ICF for Kr were provided by Sterling, Dinerstein & Kallman (2007), through detailed photoionization models. Since then, atomic data for *n*-capture ion transitions have considerably improved. New atomic data were incorporated in the new ICF computations for Kr and Se by Sterling et al. (2015). They performed a large grid of photoionization models in order to cover a considerable range of physical conditions. They derived six ICFs for Kr and three for Se, depending on which ions are detected. The quality of their Kr ICFs is confirmed by optical/IR data for 16 PNe (García-Rojas et al. 2015; Sterling et al. 2015). Thanks to the high ionization degree of the PN NGC 3918, García-Rojas et al. (2015) detected several ionization stages of Kr in the optical spectrum. Therefore, they could use the complete set of ICFs provided by Sterling et al. (2015) for Kr, finding very good agreement between all the results (see first row of their table 17). Our results for NGC 5315 are shown in Table 13. We choose the Kr abundance obtained with equation (4) of Sterling et al. (2015), because it incorporates both Kr^{2+} and Kr^{3+}. Equation (1) provides a value that is very similar to the one selected. Equation (3) produces larger Kr abundances than the best empirical estimate when $Ar^{3+}/Ar < 0.20$ (Sterling et al. 2015), which is the case of NGC 5315. The value provided by equation (2) is consistent within the uncertainties with those derive from equation (4), but it has large error bars, owing to the uncertainty in the Ar abundance.

Selenium abundances were computed using all the ICFs proposed by Sterling et al. (2015). The ICF of equation (7) is based only on Se^{2+} ionic abundance, which is uncertain due to the weakness of the [Se III] 1.0992 μm line; equation (8) provides an ICF that only considers Se^{3+} and gives a value which is much lower than those provided by the other equations. Sterling et al. (2015) argue that equation (8) is the most uncertain of the Se ICFs, due to the lack of a strong correlation with fractional abundances of light element ions. We adopt the Se abundance derived with equation (9) of Sterling et al. (2015), which is the most accurate since it takes into account both Se^{2+} and Se^{3+}. Furthermore, the unblended line of [Se III] at 1.0992 μm, first identified by Sterling et al. (2017), allows for improved accuracy of Se abundances in PNe. The Se abundances derived with the various ICFs of Sterling et al. (2015) are shown in Table 13.

At present, there are no reliable ICFs for Xe, Br and Rb available in the literature. We calculated the total abundance of Xe using equation (3) of Sterling et al. (2015) as the ICF, given the similarity between the IPs of Xe^{3+} and Kr^{3+}. Our analysis yields a higher enrichment of Xe than for Kr (0.86 dex relative to Ar, compared to 0.02 dex for Kr), but we emphasize the uncertainty of the Xe abundance. First, equation (3) of Sterling et al. (2015) gives systematically high Kr abundances in low- and moderate-excitation PNe (including NGC 5315) compared to other ICFs. We believe that this excitation effect plays a significant role in the anomalously

Table 14. N/O and C/O ratios in NGC 5315.

N/O	C/O	Reference
$0.59^{+0.24}_{-0.15}$	0.76 ± 0.13	This paper
0.41	0.64	Dufour et al. (2015)
0.89	–	Milingo et al. (2010)
0.93	0.95	Peimbert et al. (2004)
0.47	0.58	Tsamis et al. (2004)
0.54	0.35	Tsamis et al. (2003)
0.88	0.85	Pottasch et al. (2002)
0.48	–	Liu et al. (2001)
0.59	–	Samland et al. (1992)
0.36	–	de Freitas Pacheco et al. (1991)

large Xe abundance we derive. Secondly, the [Xe IV] λ7535.40 line is marginally detected, and [Xe IV] λ5709.21 not at all, resulting in a quite uncertain Xe^{3+}/H^+ ionic abundance.

As we discussed in Section 3.1, we possibly detect [Br III] λ6556.56. Since the IP of Br^{2+} is similar to the IP of Se^{2+}, we calculated the total abundance of Br by using equation (7) of Sterling et al. (2015). The Br abundance is shown in Table 12. The flux of the line detected at 6555.56 Å gives a Br^{2+} abundance much higher than expected, given the nearly solar abundances of the adjacent elements Se and Kr. We inspected the spectra to check possible contamination or alternative identifications for the feature at 6555.56 Å, but we did not find any transition with other detections belonging to the same multiplet in our spectra. We also computed an upper limit to the Br^{2+}/H^+ abundance from [Br III] $\lambda \sim 6130.40$, which we did not detect. This upper limit gives a bromine abundance < 2.43, more than an order of magnitude lower than that derived from λ6556.56. This result suggests that the [Br III] λ6556.56 is contaminated and/or incorrectly identified in NGC 5315, and we conclude that our derived Br abundance is not reliable.

Finally, from an upper limit flux estimation of the [Rb IV] λ5759.55 line, we computed an upper limit (3σ) abundance for Rb^{3+}. Considering the similarity with the IP range of O^{2+}, we used the ionization correction scheme $Rb/Rb^{3+} = O/O^{2+}$ (Sterling et al. 2016).

7 DISCUSSION

7.1 CNO abundances

The N/O and the C/O ratios are crucial for investigating the nature of PN progenitor stars. In particular, the C/O ratio is an indicator of the chemistry of the nebula (Sterling & Dinerstein 2008, and references therein) and it reveals crucial information about TDU events during the thermally pulsing AGB. The N/O ratio is a sensitive probe of HBB at the base of the convective envelope, which only occurs in stars with masses $\gtrsim 3$–$4 \, M_{\odot}$. In this section, we compare our determinations with those from the literature (see Table 14) both to assess the accuracy of our abundances as well as to utilize information from other spectral regions.

Prior to our study, the deepest optical spectrum of NGC 5315 was that analysed by Peimbert et al. (2004). They computed N/O = 0.93 using a combination of ORLs and CELs, and C/O = 0.93 from ORLs, assuming that temperature fluctuations are responsible for the ADFs. Torres-Peimbert & Peimbert (1977) assumed the temperature fluctuations paradigm in their calculations and found N/O = 0.95 from optical observations. Similarly high N/O ratios were found by Pottasch et al. (2002) and Milingo et al. (2010). In particular, Pottasch et al. (2002) used UV observations in which [N III]

and [N IV] were detected. Along with optical data, these detections allowed them to compute the total N abundance by summing the N^+, N^{2+} and N^{3+} ionic abundances, eliminating the need for an ICF.

However, not all authors have found such large N/O ratios. Tsamis et al. (2003) utilized *IUE*, optical and infrared data to compute N/O = 0.54 from CELs, although their C/O = 0.35 is lower than our derived value. This group also determined abundances from ORLs (Tsamis et al. 2004), finding N/O = 0.47 and C/O = 0.58. Dufour et al. (2015) used long-slit *HST*–STIS co-spatial UV-optical spectra and computed N/O = 0.41, which is somewhat lower than our derived value and C/O = 0.64 which is consistent with our C/O ratio; the combination of optical and UV data allowed them to avoid using ICFs. Liu et al. (2001) found N/O = 0.48 from a far-infrared *ISO* spectrum. Finally, de Freitas Pacheco et al. (1991) and Samland et al. (1992) derived N/O = 0.36 and N/O = 0.59, respectively, from low-resolution optical spectra.

The discrepancy seen in the N/O ratios calculated in the literature can be ascribed to various factors, including the temperature sensitivity of UV N III] and N IV] emission lines, and the large and uncertain ICFs required for optical spectra in which [N II] is the only N ion with CELs. However, the average value calculated from the literature is N/O = 0.63, which is consistent within the uncertainties with our result (N/O = $0.59^{+0.24}_{-0.15}$).

On the other hand, C/O ratios from both ORLs and CELs seem to agree better, with the exception of the low value found by Tsamis et al. (2003) (Table 14). All extant C/O determinations are below unity, indicating that NGC 5315 has an oxygen-rich chemistry. Interestingly, this PN exhibits both O-rich crystalline silicate dust emission features and polycyclic aromatic hydrocarbon (PAH) features that are often associated with C-rich chemistries (Cohen & Barlow 2005). This dual-dust chemistry has been found in other PNe with [WC] central stars (e.g. Perea-Calderón et al. 2009) and may be associated with binary interactions (de Marco & Soker 2002).

Oxygen-rich PNe can be associated either with low mass stars ($M < 1.5 \, M_{\odot}$), in which TDU events did not occur (preventing C enrichment on the stellar surface), or with massive stars (M > 3–$4 \, M_{\odot}$), where the temperature at the base of the convective envelope is high enough to active HBB. In the latter case, C is converted to N by the CN cycle, leading to N and He enrichments.

Peimbert Type I PNe exhibit N and/or He enrichments typical of HBB, and hence are believed to be descendants of more massive AGB stars. This is supported by statistical evidence based on the scaleheights, large central star masses and high central star temperatures of Type I PNe (e.g. Peimbert 1990; Corradi & Schwarz 1995; Gorny, Stasińska & Tylenda 1997; Stanghellini et al. 2002; Peña, Rechy-García & García-Rojas 2013). Several different criteria have been proposed for Type I classification in the literature. The initial criterion defined by Peimbert (1978) was overly restrictive because of the overestimation of He abundances and of electron temperatures which led to artificially large N/O ratios. Therefore, Peimbert & Torres-Peimbert (1983) refined these thresholds and defined Type I PNe as those having He/H > 0.125 or N/O > 0.5. Later, Maciel & Quireza (1999) required that both of these thresholds be met for Type I classification. Kingsburgh & Barlow (1994) proposed that Type I PNe can be classified on the basis of the N/O ratio alone, with the minimum N/O given by (C+N)/O in H II regions of the host galaxy. In the solar neighbourhood, this limit is N/O > 0.8. Based on more recent H II region and solar abundances, Henry, Kwitter & Balick (2004) refined this criterion to N/O $\geq$ 0.65.

Our He/H (0.129 ± 0.009) and N/O ($0.59^{+0.24}_{-0.15}$) abundance determinations indicate that NGC 5315 is a Type I PN according to
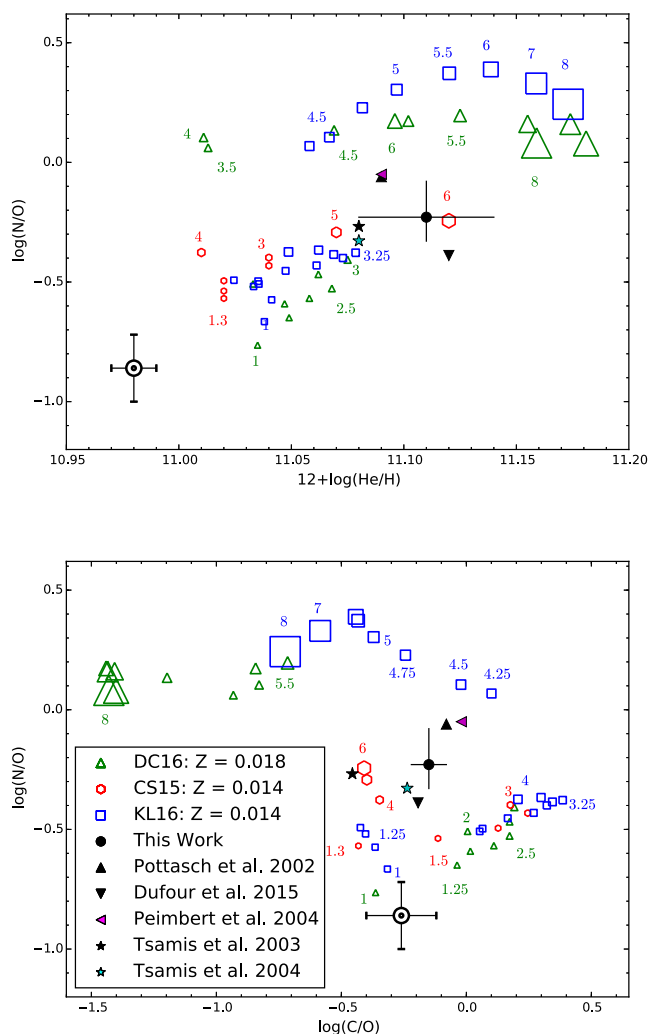
Figure 5. Upper panel: N/O versus He/H ratios predicted by nucleosynthesis models. Lower panel: N/O versus C/O ratios. In both plots, blue squares are the values predicted by Karakas & Lugaro (2016) nucleosynthesis models, green triangles from Di Criscienzo et al. (2016) nucleosynthesis models and red hexagons from Cristallo et al. (2015) nucleosynthesis models. Sizes of the symbols are scaled to the progenitor masses. Some labels have been included to help the reader to interpret the plots. The black dots are the observational results from our analysis. For comparison, we include abundance ratios from the literature.

the Maciel & Quireza (1999) criterion, but not according to Henry et al. (2004). The uncertainties are sufficiently large so that we cannot classify this PN either as a Type I or as a non-Type I with confidence. Literature abundances are similarly inconclusive (Table 14). Nevertheless, it appears that NGC 5315 experienced some N and He enrichments, but HBB apparently did not operate efficiently in its progenitor. This suggests that the progenitor of NGC 5315 may have had an initial mass $M \approx 3$–5 M$_\odot$. However, in this mass range the cessation of HBB can occur before the end of the thermally pulsing AGB phase, and subsequent TDU episodes can lead to carbon enrichment (e.g. Frost et al. 1998; Ventura et al. 2015).

To shed more light on the nature of the progenitor star, we compare our abundances with the nucleosynthetic models of Karakas & Lugaro (2016, hereafter KL16), Di Criscienzo et al. (2016, hereafter DC16) and Cristallo et al. (2015, hereafter CS15). In Fig. 5, we show the predicted N/O versus He/H ratios and N/O versus C/O ratios for different progenitor masses with solar or near-solar metallicity,

compared with our observed values. In the N/O versus He/H plot, the mass of the progenitor star of NGC 5315 is consistent, within the uncertainties, with predictions for 3–3.5 M$_\odot$ stars according to the predictions of KL16 and DC16. The CS15 models do not predict HBB at these masses at solar metallicities, and the predicted mass in this case is higher (5.5–6 M$_\odot$). Literature abundances generally agree with this assessment, although the Pottasch et al. (2002) and Peimbert et al. (2004) data suggest a higher initial mass of 4.5–6.0 M$_\odot$ on account of their larger N/O ratios. On the other hand, our N/O and C/O abundances (lower panel of Fig. 5) are not consistent with model predictions, except possibly for 1–1.5 M$_\odot$ values of KL16. Literature abundances show a dichotomy, with those having larger N/O ratios closer to the 4–5 M$_\odot$ predictions of KL16, and those with smaller N/O agreeing more with 4–6 M$_\odot$ predictions from CS15 or KL16's 1–1.5 M$_\odot$ values.

Therefore, light element abundances do not significantly constrain the progenitor mass of NGC 5315, other than to suggest that an initial mass of 2–3 M$_\odot$ is unlikely. It should be noted that while He and N are moderately enriched, as may be expected for a more massive progenitor, extra mixing processes in less massive stars during the RGB and AGB phases can also produce such enrichments (Nollett, Busso & Wasserburg 2003).

7.2 Neutron-capture element abundances

The pattern of s-process enrichments of n-capture elements, or lack thereof, can also provide information about the nature of PN progenitor stars. To assess whether the s-process and TDU occurred during the AGB, it is necessary to assume an initial abundance pattern and to adopt a metallicity reference element. For Galactic disc PNe such as NGC 5315, scaled solar abundances are usually a reasonable approximation (Henry et al. 2004). Historically, O was used as reference element in non-Type I PNe, while in Type I PNe Ar turns out to be the best choice if O is affected by nucleosynthesis in the progenitor star of these objects (Sterling & Dinerstein 2008; Karakas et al. 2009). Moreover, Delgado-Inglada et al. (2015) have found evidence for O enrichment in Galactic PNe with carbon-rich dust, suggesting that, in general, Ar or Cl are better reference elements. A positive value of [X/(O, Ar)],[3] where X is a n-capture element, indicates that the progenitor star experienced s-process enrichment. We use Asplund et al. (2009) as the reference for the Solar abundances.

In Table 15, we show the average value of Se and Kr enrichments found by Sterling et al. (2015) in their sample of Type I and non-Type I PN, compared with NGC 5315 and García-Rojas et al. (2015)'s results for NGC 3918. Given the difficulty of classifying NGC 5315 as a Type I or non-Type I PN, we decided to calculate enrichments using Ar as reference element, and we chose the same reference for the sample of García-Rojas et al. (2012, 2015). We find that Kr and Se are not enriched, in contrast to the C-rich NGC 3918 García-Rojas et al. (2015).

Rb is another key element for diagnosing s-process nucleosynthesis, as it is an indicator of the main neutron source during the AGB phase. A large enrichment of Rb relative to other n-capture elements indicates that ^{22}Ne is the dominant reaction for the production of neutrons. In this case, the high neutron density activates different branching points in the s-process path, increasing the production of Rb and Kr (Abia et al. 2001; Karakas et al. 2012; van

---

[3] The notation [X/Y] represents the logarithmic difference between nebular and solar ratio abundances, i.e. $[X/Y] = \log(X/Y) - \log(X/Y)_\odot$.

Table 15. Neutron-capture element abundances.

	NGC 5315	NGC 3918[a]	<Type I PNe>[b]	<Non-Type I PNe>[b]
[Se/(O, Ar)]	-0.07 ± 0.29	0.19	-0.01	0.20
[Kr/(O, Ar)]	0.02 ± 0.26	0.68	0.13	0.91
[Br/(O, Ar)]	0.66:	–	–	–
[Rb/(O, Ar)]	<0.02	>0.00	–	–
[Xe/(O, Ar)]	0.86:	>0.26	–	–

Notes. [a]García-Rojas et al. (2015).
[b]Mean values from the sample of Sterling et al. (2015).

Raai et al. 2012). According to models, stars with $M > 5 \, M_\odot$ attain the temperatures required for the activation of the reaction ^{22}Ne(α, n)^{25}Mg (Busso et al. 1999), and thus Rb is an indicator of the mass of the progenitor star (see Section 1). We do not detect Rb in NGC 5315, but compute a 3σ upper limit of [Rb/Ar] < 0.02. The lack of enrichment agrees with the Se and Kr abundances, and suggests that the progenitor of NGC 5315 is less than $6 \, M_\odot$ (Karakas & Lugaro 2016).

Our Br and Xe abundances (see Table 15) must be taken with caution. The identification of the $\lambda6556$ line as [Br III] is questionable, as discussed in Section 6.1. In the case of Xe, we marginally detected one line, [Xe IV] $\lambda7535.40$. For lack of Xe ICFs, we use equation (3) of Sterling et al. (2015) to compute the Xe abundance. This ICF is known to produce systematically high ICFs in low- and moderate-excitation PNe, as was found specifically for NGC 5315. For this reason, we believe that the derived Xe abundance is overestimated by ~0.60 dex, based on our results for Kr (Table 13).

The lack of s-process enrichments indicate that the progenitor of NGC 5315 either was a low-mass star ($M < 1.5 \, M_\odot$) or an intermediate-mass star ($3 \, M_\odot < M < 6 \, M_\odot$).

The lack of carbon enrichment is consistent with our derived n-capture element abundances. Theoretical low-to-intermediate mass stellar evolution models predict a correlation between n-capture element and C enrichment in PNe, as they are processed in the same stellar layers and dredged up together to the surface during TDU episodes (Gallino et al. 1998; Busso et al. 2001, KL14). In Fig. 6, we plot the correlation between C/O and [Kr/Ar] for PNe with the most accurate Kr abundances (derived from multiple Kr ions, see Sterling et al. 2015). We find evidence for a correlation, given by

$$[\text{Kr/Ar}] = (0.415 \pm 0.169) + (0.671 \pm 0.453)\log(\text{C/O}). \quad (1)$$

New optical/NIR observations will be necessary to expand the sample and to strengthen this result, and search for correlations between C/O ratios and other n-capture elements.

7.3 The enigmatic progenitor star of NGC 5315

Armed with our abundance analysis, we now consider the various scenarios for the nature of the progenitor of NGC 5315. The result is rather unsatisfying, as we cannot discriminate between a low-mass and intermediate-mass origin for the progenitor. The O-rich chemistry and lack of s-process enrichment only seem to rule out the mass range $1.5 \, M_\odot < M < 3.0 \, M_\odot$, according to single star evolution. The conclusions are even less restrictive if binary interactions led to the formation of NGC 5315 – although there is evidence that this indeed may be the case, as outlined below.

We find three viable evolutionary channels for the progenitor of NGC 5315.
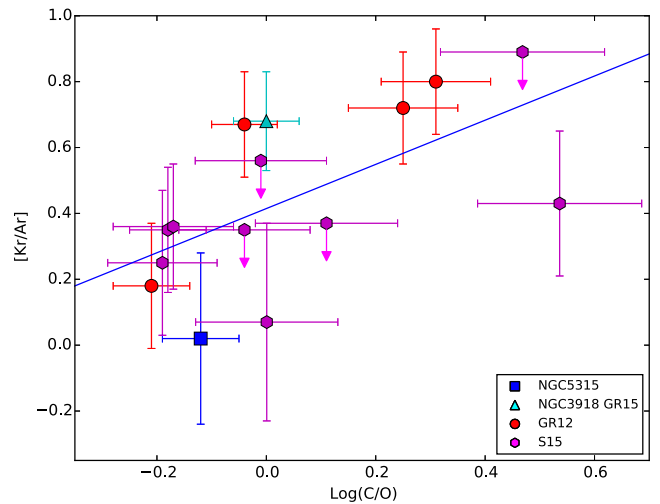
Figure 6. Correlation between Kr and C enrichment, using solar abundances by Asplund et al. (2009). In this plot, Kr enrichment is measured using Ar for all the PNe. The linear fit to the data is shown as a blue line. We have not considered upper limits to compute the fit. C/O ratios are computed from ORLs. Labels are the following – GR15: García-Rojas et al. (2015); GR12: García-Rojas et al. (2012); S15: Sterling et al. (2015).

(*i*) The intermediate-mass star scenario. NGC 5315 exhibits moderate enrichments of He and N, as may be expected for a more massive progenitor star that underwent HBB. However the N/O ratio appears to fall below the Type I PN classification criteria, indicating that HBB did not modify its composition to a substantial extent. The comparison between observed and predicted N/O and He abundances are consistent within the uncertainties with a progenitor mass of $3–5 \, M_\odot$, depending on the AGB models used. However, in the C/O versus N/O plane, the measured abundances are consistent with an intermediate-mass progenitor only for the model predictions of Cristallo et al. (2015). Comparison with the Karakas & Lugaro (2016) predictions instead indicate a low-mass progenitor ($M < 1.5 \, M_\odot$). Sterling et al. (2015) found a lack of s-process enrichments of Se and Kr in Type I PNe, perhaps due to the relatively small intershell mass and/or strong dilution of enriched material into the massive envelopes of the AGB progenitor stars. The lack of s-process enrichments in NGC 5315 is consistent with this scenario.

(*ii*) The low-mass progenitor scenario. The lack of s-process enrichments and O-rich chemistry of the nebula can be equally well ascribed to a low-mass progenitor ($M < 1.5 \, M_\odot$ Karakas & Lugaro 2016, and references therein) that did not experience the s-process or TDU. The He and N enrichments can be produced by extra mixing processes in low-mass stars during the RGB and the AGB phase (Nollett et al. 2003), although the nature of these phenomena are not well understood (e.g. Karakas & Lugaro 2016).

Additional support is provided by indirect estimates of the central star mass. Using a luminosity based on the extinction distance, Pottasch & Bernard-Salas (2010) estimate $M \leq 1.5\,M_{\odot}$ when comparing with post-AGB evolutionary tracks. From photoionization models, Henry et al. (2015) estimated the central star luminosity and used evolutionary tracks to determine a progenitor mass of $1.1\,M_{\odot}$. Both of these mass estimates carry caveats. The abundance analysis of Pottasch & Bernard-Salas (2010) indicated a much larger progenitor mass of $M = 4.5\,M_{\odot}$. The mass derived by Henry et al. (2015) is strongly model dependent, and their stellar luminosity disagrees both with the statistical distance determinations and with the extinction distance of Pottasch & Bernard-Salas (2010). Further evidence against this scenario comes from α-element abundances. Because low-mass stars have longer lifetimes, the abundances of elements such as Cl and Ar should be lower than in Galactic H II regions. Esteban et al. (2015) determined $12+\log (<\mathrm{Cl/H}>) = 5.09$ and García-Rojas & Esteban (2007) found $12+\log(<\mathrm{Ar/H}>) = 6.52$ in H II regions, which are lower than we find for NGC 5315. Furthermore, we compare our O, Cl and Ar abundances with the averaged values from a large sample of Type II PNe analysed by Kwitter & Henry (2001). They found lower abundances than our results for elements unaffected by stellar nucleosynthesis: $12+\log (<\mathrm{O/H}>) = 8.74$, $12+\log (<\mathrm{Cl/H}>) = 5.28$ and $12+\log (<\mathrm{Ar/H}>) = 6.45$, suggesting that the progenitor star of NGC 5315 was formed more recently and hence is probably descent from a more massive progenitor star.

(*iii*) The binary progenitor scenario. The peculiar multipolar morphology of NGC 5315 can be produced by binary interactions during the AGB (Balick & Frank 2002; de Marco 2009; Hillwig et al. 2016, and references therein). Mass transfer can reduce the envelope mass of the AGB star and prematurely truncate the AGB lifetime before significant C and s-process enrichments can occur. Depending on the orbit of the binary companion, the N and He enrichments could have been produced by HBB, or by extra mixing (or some other mixing process triggered by binary interactions) (Nollett et al. 2003). This scenario is supported by the findings of Manick, Miszalsky & McBride (2015), who conducted a detailed study of RV variations of a sample of central stars of PNe. They found a strong RV variation for the central star of NGC 5315, which may be explained with the presence of a close companion. Manick et al. (2015) emphasize that this result is preliminary because their observations only include four epochs, which is not sufficient to conclude that it has a periodic RV variation typical of binary systems. A further complication is the Wolf–Rayet central star itself, whose stellar wind could produce RV variations. A binary central star can also explain the dual-dust chemistry of NGC 5315 and other PNe with [WC] central stars (de Marco & Soker 2002; Cohen & Barlow 2005; Perea-Calderón et al. 2009). Finally, a binary origin could help to bridge the dissonance between progenitor mass estimates from abundances and from other methods (Pottasch & Bernard-Salas 2010).

We speculate that NGC 5315 most likely had a binary progenitor star, although we cannot dismiss the first two scenarios. The combination of RV variations, PAH and silicate dust emission features, and an overall lack of agreement between observed and predicted abundances support this scenario. The moderate N and He enrichments and Rb upper limit suggest that NGC 5315 could not have had a (single) progenitor mass above $\sim5\,M_{\odot}$. HBB can cease before the thermally pulsing AGB phase is over, allowing for TDU to produce C and s-process enrichments (Frost et al. 1998; Ventura et al. 2015). The α-element abundances of NGC 5315 suggest that a low-mass progenitor [$M < 1.5\,M_{\odot}$, scenario (*ii*)] is unlikely.

However, more data are needed to reveal the nature of NGC 5315's progenitor star. Specifically, observations are needed to test whether the RV variations found by Manick et al. (2015) are periodic. If the central star indeed has a binary companion, its orbital characteristics can be used to constrain the likelihood of mass transfer during the AGB. Furthermore, a detailed analysis and modelling of the [WC4] central star (e.g. Koesterke & Hamann 1997) can constrain the stellar luminosity and hence mass. Marcolino et al. (2007) and Todt et al. (2015) used detailed stellar atmosphere codes which are appropriate when non-LTE conditions and stellar winds are present. However, as the distance estimates to Galactic PNe are unreliable, they assumed a 'standard' luminosity for their models and scale their results to other luminosities through a transformed radius (see Todt et al. 2015). The upcoming *GAIA* data release of precise parallaxes will turn around this behaviour. This information can be used to more accurately estimate the initial mass than has been possible.

These different scenarios highlight other open questions. The origin of non-spherical PNe has always been a matter of debate. There is still no quantitative theory to explain how a massive single star can form a highly non-spherical PN. The multipolar morphology can be explained with central binary systems, but only in a small fraction of them the orbital period is short enough to allow the companion to interact with the AGB star and modify the morphology of the PN (de Marco & Izzard 2017). Therefore, the small fraction of single massive stars and compact binary systems cannot explain the high concentration of non-spherical PNe [≈80 per cent; Parker et al. (2006)]. Another unresolved problem concerns the large percentage of Type I PNe [≈20 per cent; Kingsburgh & Barlow (1994)]. The IMF suggests that stars with $M > 3\,M_{\odot}$ are only a few per cent of the total population of our Galaxy. Therefore, the question is how many Type I PNe come from high mass progenitor stars? Rb abundance determinations in Type I PNe are urgently needed to verify which Type I PNe are descendants of the Rb-rich AGB stars observed by García-Hernández et al. (2006, 2009). Finally, a crucial point for future works is to investigate whether high N and He abundances can be understood in the framework of binary interactions and/or extra mixing in low (or intermediate) mass stars.

8 SUMMARY AND CONCLUSIONS

We analysed the high-resolution ($R \sim 40\,000$) optical spectrum obtained with UVES at the Very Large Telescope, and the medium-resolution ($R \sim 4800$) near-infrared spectrum with FIRE at MBT of NGC5315. We detect, identify and measure the intensities of about 700 lines in both spectra. Physical conditions were computed using intensity ratios of common ions. Ionic abundances were computed for ions which present available atomic data. Elemental abundances of common elements (O, Ar, Cl, N, S, ...) were performed using the more recent ICFs available when needed. The total abundances of n-capture elements were calculated for Kr, Se, Xe, Br and Rb, using sophisticated ICFs for Kr and Se and the best approximate correction scheme for Xe, Br and Rb. Finally, the enrichment of these elements was measured, using Ar as reference element, against solar abundances.

The aim of this work was to study the s-process in the progenitor of the PN NGC 5315. The relatively high concentration of N and He computed, may be associated with the occurrence of HBB and second dredge up, which are activated in AGB stars with $M > 3$–$4\,M_{\odot}$. Nevertheless, extra mixing events, thermohaline mixing (Eggleton et al. 2006) and magnetic buoyancy (Trippella et al. 2014) in less massive stars during first and TDU may also enhance the final amount of N and He. The causes of these processes are still poorly known. Furthermore, the multipolar morphology and dual-dust chemistry of NGC 5315 may be explained with the

presence of a central binary system. Taking in account these considerations, we suggest that the most reasonable interpretation to the observed chemical abundances and for the absence of s-process enrichment in NGC 5315 is that a central binary system can be the cause of a poor or absent s-process enrichment, due to a strong interaction with a close companion that can reduce the AGB lifetime through mass transfer. However, we cannot rule out other two alternative interpretations: (i) that this PN descend from a progenitor star with mass between 3 and 5 $M_\odot$, where the massive convective envelope dilutes the n-capture enrichment during TDU events and the intershell region between He- and H-burning shells is smaller than in lower mass stars; (ii) finally, a low mass progenitor star ($M < 1.5\,M_\odot$) that did not experience TDU, and the stellar surface is not enriched in s-processed material.

Our FIRE spectrum allows us to test the complete set of Se ICFs developed by Sterling et al. (2015). We consider the ICF given by their equation (9), which considers two different ions, as representative of Se total abundance. The identification of the non-blended [Se III] $\lambda 1.0995\,\mu m$ line provides a much more robust test for the Se ICFs, than the blended [Se III] 8854 Å line.

Finally, another important theoretical prediction was tested: the correlation between Kr and C enrichment. n-capture elements are formed in the same layers of C, both are dredged up together to the stellar surface during TDU episodes and then stellar winds and PN ejections expel them in the interstellar medium. Therefore, we expect a correlation which is shown in Fig. 6.

ACKNOWLEDGEMENTS

REFERENCES

Abia C., Busso M., Gallino R., Domínguez I., Straniero O., Isern J., 2001, ApJ, 559, 1117
Asplund M., Grevesse N., Sauval A. J., Scott P., 2009, ARA&A, 47, 481
Balick B., Frank A., 2002, ARA&A, 40, 439
Barlow M. J., Liu X.-W., Péquignot D., Storey P. J., Tsamis Y. G., Morisset C., 2003, in Kwok S., Dopita M., Sutherland R., eds, Proc. IAU Symp. 209, Planetary Nebulae: Their Evolution and Role in the Universe. Astron. Soc. Pac., San Francisco, p. 373
Bautista M. A., Fivet V., Ballance C., Quinet P., Ferland G., Mendoza C., Kallman T. R., 2015, ApJ, 808, 174
Becker S. R., Iben I., Jr, 1979, ApJ, 232, 831
Biémont E., Hansen J. E., 1986a, Phys. Scr., 34, 116
Biémont E., Hansen J. E., 1986b, Phys. Scr., 33, 117
Biémont E., Hansen J. E., Quinet P., Zeippen C. J., 1995, A&AS, 111, 333
Blum R. D., McGregor P. J., 2008, AJ, 135, 1708

Bochanski J. J. et al., 2009, PASP, 121, 1409
Boothroyd A. I., Sackmann I.-J., Ahern S. C., 1993, ApJ, 416, 762
Busso M., Gallino R., Wasserburg G. J., 1999, ARA&A, 37, 239
Busso M., Gallino R., Lambert D. L., Travaglio C., Smith V. V., 2001, ApJ, 557, 802
Butler K., Zeippen C. J., 1989, A&A, 208, 337
Cahn J. H., Kaler J. B., Stanghellini L., 1992, A&AS, 94, 399
Cardelli J. A., Clayton G. C., Mathis J. S., 1989, ApJ, 345, 245
Cohen M., Barlow M. J., 2005, MNRAS, 362, 1199
Corradi R., Schwarz H. E., 1995, A&A, 293, 871
Cristallo S., Piersanti L., Straniero O., Gallino R., Domínguez I., Abia C., Quintini M., Bisterzo S., 2011, ApJS, 197, 17
Cristallo S., Straniero O., Piersanti L., Gobrecht D., 2015, ApJS, 219, 40
de Freitas Pacheco J. A., Maciel W. J., Costa R. D. D., Barbuy B., 1991, A&A, 250, 159
de Marco O., 2009, PASP, 121, 316
de Marco O., Izzard R. G., 2017, PASP, 34, e001
de Marco O., Soker N., 2002, PASP, 114, 602
Davey A. R., Storey P. J., Kisielius R., 2000, A&AS, 142, 85
Delgado-Inglada G., Rodríguez M., 2014, ApJ, 784, 173
Delgado-Inglada G., Morisset C., Stasińska G., 2014, MNRAS, 440, 536 (D-I14)
Delgado-Inglada G., Rodríguez M., Peimbert M., Stasińska G., Morisset C., 2015, MNRAS, 449, 1797
Di Criscienzo M. et al., 2016, MNRAS, 462, 395
Dinerstein H. L., 2001, ApJ, 550, L223
D'Odorico S., Cristiani S., Dekker H., Hill V., Kaufer A., Kim T., Primas F., 2000, in Bergeron J., ed., Proc. SPIE Conf. Ser. 4005, Discoveries and Research Prospects from 8- to 10-Meter-Class Telescopes. SPIE, Bellingham, p. 121
Dufour R. J., Kwitter K. B., Shaw R. A., Henry R. B. C., Balick B., Corradi L. M., 2015, ApJ, 803, 23
Eggleton P. P., Dearborn D. S. P., Lattanzio J. C., 2006, Science, 314, 1580
Ellis D. G., Martinson I., 1984, Phys. Scr., 30, 255
Escalante V., Morisset C., Georgiev L., 2012, MNRAS, 426, 2318
Esteban C., Peimbert M., Torres-Peimbert S., Escalante V., 1998, MNRAS, 295, 401
Esteban C., Peimbert M., García-Rojas J., Ruiz M. T., Peimbert A., Rodríguez M., 2004, MNRAS, 355, 229
Esteban C., García-Rojas J., Pérez-Mesa V., 2015, MNRAS, 452, 1553
Fang X., Storey P. J., Liu X.-W., 2011, A&A, 530, A18
Fang X., Storey P. J., Liu X.-W., 2013, A&A, 550, C2
Ferland G. J. et al., 2013, Rev. Mex. Astron. Astrofis., 49, 137
Froese Fischer C., Tachiev G., 2004, At. Data Nucl. Data Tables, 87, 1
Frost C. A., Cannon R. C., Lattanzio J. C., Wood P. R., Forestini M., 1998, A&A, 332, L17
Galavís M. E., Mendoza C., Zeippen C. J., 1995, A&AS, 111, 347
Galavís M. E., Mendoza C., Zeippen C. J., 1997, A&AS, 123, 159
Gallino R., Arlandini C., Busso M., Lugaro M., Travaglio C., Straniero O., Chieffi A., Limongi M., 1998, ApJ, 497, 388
García-Hernández D. A., García-Lario P., Plez B., D'Antona F., Manchado A., Trigo-Rodríguez J. M., 2006, Science, 314, 1751
García-Hernández D. A., García-Lario P., Plez B., Manchado A., D'Antona F., Lub J., Habing H., 2007, A&A, 462, 711
García-Hernández D. A., Manchado A., Lambert D. L., Plez B., García-Lario P., D'Antona F., Lugaro M., Karakas A. I., van Raai M. A., 2009, ApJ, 705, L31
García-Hernández D. A., Zamora O., Yagüe A., Uttenthaler S., Karakas A. I., Lugaro M., Ventura P., Lambert D. L., 2013, A&A, 555, 3
García-Rojas J., Esteban C., 2007, ApJ, 670, 457
García-Rojas J., Peña M., Morisset C., Mesa-Delgado A., Ruiz M. T., 2012, A&A, 538, A54
García-Rojas J., Madonna S., Luridiana V., Sterling N. C., Morisset C., Delgado-Inglada G., Toribio San Cipriano L., 2015, MNRAS, 452, 2606
García-Rojas J., Corradi R., Romano L. M., Monteiro H., Jones D., Rodríguez-Gil P., Cabrera-Lavers A., 2016, ApJ, 824, L27
Gorny S. K., Stasińska G., Tylenda R., 1997, A&A, 318, 256
Hamuy M., Walker A. R., Suntzeff N. B., Gigoux P., Heathcote S. R., Phillips M. M., 1992, PASP, 104, 533

Hamuy M., Suntzeff N. B., Heathcote S. R., Walker A. R., Gigoux P., Phillips M. M., 1994, PASP, 106, 566

Hanuschik R. W., 2003, A&A, 407, 1157

Henry R. B. C., Kwitter K. B., Balick B., 2004, AJ, 127, 2284

Henry R. B. C., Balick B., Dufour R. J., Kwitter K. B., Shaw R. A., Miller T. R., Buell J. F., Corradi R. L. M., 2015, ApJ, 813, 121

Hillwig T. C., Jones D., De Marco O., Bond H. E., Margheim S., Frew D., 2016, ApJ, 832, 125

Hora J. L., Latter W. B., Deutsch L. K., 1999, ApJS, 124, 195

Johansson S., Zethson T., Hartman H., Ekberg J. O., Ishibashi K., Davidson K., Gull T., 2000, A&A, 361, 977

Karakas A. I., Lattanzio J. C., 2014, PASA, 31, 62

Karakas A. I., Lugaro M., 2016, ApJ, 825, 26 (KL16)

Karakas A. I., van Raai M. A., Lugaro M., Sterling N. C., Dinerstein H. L., 2009, ApJ, 690, 1130

Karakas A. I., García-Hernández D. A., Lugaro M., 2012, ApJ, 751, 8

Kaufman V., Sugar J., 1986, J. Phys. Chem. Ref. Data, 15, 321

Kingsburgh R. L., Barlow M. J., 1994, MNRAS, 271, 257

Kisielius R., Storey P. J., Davey A. R., Neale L. T., 1998, A&AS, 133, 257

Kisielius R., Storey P. J., Ferland G. J., Keenan F. P., 2009, MNRAS, 397, 903

Koesterke L., Hamann W.-R., 1997, A&A, 320, 91

Kwitter K. B., Henry R. B. C., 2001, ApJ, 562, 804

Liu X.-W., Storey P. J., Barlow M. J., Clegg R. E. S., 1995, MNRAS, 272, 369

Liu X.-W., Storey P. J., Barlow M. J., Danziger I. J., Cohen M., Bryce M., 2000, MNRAS, 312, 585

Liu X.-W. et al., 2001, MNRAS, 323, 343

Luridiana V., Morisset C., Shaw R. A., 2015, A&A, 573, A42

McLaughlin B. M., Bell K. L., 2000, J. Phys. B: At. Mol. Opt. Phys., 33, 597

Maciel W. J, Quireza C., 1999, A&A, 345, 629

Manick R., Miszalsky B., McBride V., 2015, MNRAS, 448, 1789

Marcolino W. L. F., Hillier D. J., de Araujo F. X., Pereira C. B., 2007, ApJ, 654, 1068

Mashburn A. L., Sterling N. C., Madonna S., Dinerstein H. L., Roederer I. U., Geballe T. R., 2016, ApJ, 831, 3

Mendoza C., 1983, in Flower D. R., ed., Proc. IAU Symp. 103, Planetary Nebulae. Reidel, Dordrecht, p. 143

Mendoza C., Zeippen C. J., 1982a, MNRAS, 199, 1025

Mendoza C., Zeippen C. J., 1982b, MNRAS, 198, 127

Mendoza C., Zeippen C. J., 1983, MNRAS, 202, 981

Milingo J. B., Kwitter K. B., Henry R. B. C., Souza S. P., 2010, ApJ, 711, 619

Nicholls D. C., Dopita M. A., Sutherland R. S., 2012, ApJ, 752, 148

Nollett K. M., Busso M., Wasserburg G. J., 2003, ApJ, 582, 1036

Oke J. B., 1990, AJ, 99, 1621

Oliva E. et al., 2015, A&A, 581, 47

Parker Q. A. et al., 2006, MNRAS, 373, 79

Peimbert M., 1967, ApJ, 150, 825

Peimbert M., 1978, in Terzian Y., ed., Proc. IAU Symp. 76, Planetary Nebulae. Reidel, Dordrecht, p. 215

Peimbert M., 1990, Rep. Progr. Phys., 53, 1559

Peimbert M., Torres-Peimbert S., 1983, in Flower D. R., ed., Proc. IAU Symp., 103, Planetary Nebulae. Reidel, Dordrecht, p. 233

Peimbert M., Peimbert A., Ruiz M. T., Esteban C., 2004, ApJS, 150, 431

Peña M., Rechy-García S., García-Rojas J., 2013, Rev. Mex. Astron. Astrofis., 49, 87

Péquignot D., Baluteau J.-P., 1994, A&A, 283, 593

Perea-Calderón J. V., García-Hernández D. A., García-Lario P., Szczerba R., Bobrowsky M., 2009, A&A, 495, 5

Podobedova L. I., Kelleher D. E., Wiese W. L., 2009, J. Phys. Chem. Ref. Data, 38, 171

Porter R. L., Ferland G. J., Storey P. J., Detisch M. J., 2012, MNRAS, 425, L28

Porter R. L., Ferland G. J., Storey P. J., Detisch M. J., 2013, MNRAS, 433, L89

Pottasch S. R., Bernard-Salas J., 2010, A&A, 517, 95

Pottasch S. R., Beintema D. A., Bernard Salas J., Koornneef J., Feibelman W. A., 2002, A&A, 393, 285

Quinet P., 1996, A&AS, 116, 573

Ramsbottom C. A., Bell K. L., 1997, At. Data Nucl. Data Tables, 66, 65

Rodríguez M., Rubin R. H., 2005, ApJ, 626, 900

Rudy R. J., Lynch D. K., Mazuk S., Puetter R. C., Dearborn D. S. P., 2001, AJ, 121, 362

Ruiz M. T., Peimbert A., Peimbert M., Esteban C., 2003, ApJ, 595, 247

Samland M., Koeppen J., Acker A., Stenholm B., 1992, A&A, 264, 184

Schoening T., Butler K., 1998, A&AS, 128, 581

Schoning T., 1997, A&AS, 122, 277

Sharpee B., Zhang Y., Williams R., Pellegrini E., Cavagnolo K., Baldwin J. A., Phillips M., Liu X.-W., 2007, ApJ, 659, 1265

Simcoe R. A. et al., 2013, PASP, 125, 270

Stanghellini L., Villaver E., Manchado A., Guerrero M. A., 2002, ApJ, 576, 285

Sterling N. C., Dinerstein H. L., 2008, ApJS, 174, 158

Sterling N. C., Dinerstein H. L., Kallman T. R., 2007, ApJS, 169, 37

Sterling N. C., Porter R. L., Dinerstein H. L., 2015, ApJS, 218, 25

Sterling N. C., Dinerstein H. L., Kaplan K. F., Bautista M. A., 2016, ApJ, 819, 9

Sterling N. C., Madonna S., Butler K., Garcia-Rojas J., Mashburn A. L., Morisset C., Luridiana V., Roederer I. U., 2017, ApJ, 840, 80

Storey P. J., 1994, A&A, 282, 999

Storey P. J., Hummer D. G., 1995, MNRAS, 272, 41

Storey P. J., Zeippen C. J., 2000, MNRAS, 312, 813

Storey P. J., Sochi T., Badnell N. R., 2014, MNRAS, 441, 3028

Tayal S. S., 2004, A&A, 426, 717

Tayal S. S., 2011, ApJS, 195, 12

Tayal S. S., Gupta G. P., 1999, ApJ, 526, 544

Tayal S. S., Zatsarinny O., 2010, ApJS, 188, 32

Todt H. et al., 2015, in Dufour P., Bergeron P., Fontaine G., eds, ASP Conf. Ser. Vol. 493, 19th European Workshop on White Dwarfs. Astron. Soc. Pac., San Francisco, p. 539

Tody D., 1993, in Hanisch R. J., Brissenden R. J. V., Barnes J., eds, ASP Conf. Ser. Vol. 52, Astronomical Data Analysis Software and Systems II. Astron. Soc. Pac., San Francisco, p. 173

Torres-Peimbert S., Peimbert M., 1977, Rev. Mex. Astron. Astrofis., 2, 181

Torres-Peimbert S., Peimbert M., Daltabuit E., 1980, ApJ, 238, 133

Trippella O., Busso M., Maiorca E., Käppeler F., Palmerini S., 2014, ApJ, 787, 41

Trippella O., Busso M., Palmerini S., Maiorca E., Nucci M. C., 2016, ApJ, 818, 125

Tsamis Y. G., Barlow M. J., Liu X.-W., Danziger I. J., Storey P. J., 2003, MNRAS, 345, 186

Tsamis Y. G., Barlow M. J., Liu X.-W., Storey P. J., Danziger I. J., 2004, MNRAS, 353, 953

van Raai M. A., Lugaro M., Karakas A. I., García-Hernández D. A., Yong D., 2012, A&A, 540, A44

Vanzi L., Cresci G., Telles E., Melnick J., 2008, A&A, 486, 393

Ventura P., Stanghellini L., Dell'Agli F., García-Hernández D. A., Di Criscienzo M., 2015, MNRAS, 452, 3679

Wang W., Liu X.-W., 2007, MNRAS, 381, 669

Wesson R., Liu X.-W., Barlow M. J., 2005, MNRAS, 362, 424

Zamora O., García-Hernández D. A., Plez B., Manchado A., 2014, A&A, 564, L4

Zhang H., 1996, A&AS, 119, 523

This paper has been typeset from a TEX/LATEX file prepared by the author.